




## Article

# Satellite Image Restoration via an Adaptive QWNNM Model

Xudong Xu <sup>1</sup>, Zhihua Zhang <sup>1,\*</sup> and M. James C. Crabbe <sup>2</sup><sup>1</sup> Interdisciplinary Data Mining Group, School of Mathematics, Shandong University, Jinan 250100, China<sup>2</sup> Wolfson College, Oxford University, Oxford OX2 6UD, UK

\* Correspondence: zhangzhihua@sdu.edu.cn

**Abstract:** Due to channel noise and random atmospheric turbulence, retrieved satellite images are always distorted and degraded and so require further restoration before use in various applications. The latest quaternion-based weighted nuclear norm minimization (QWNNM) model, which utilizes the idea of low-rank matrix approximation and the quaternion representation of multi-channel satellite images, can achieve image restoration and enhancement. However, the QWNNM model ignores the impact of noise on similarity measurement, lacks the utilization of residual image information, and fixes the number of iterations. In order to address these drawbacks, we propose three adaptive strategies: adaptive noise-resilient block matching, adaptive feedback of residual image, and adaptive iteration stopping criterion in a new adaptive QWNNM model. Both simulation experiments with known noise/blurring and real environment experiments with unknown noise/blurring demonstrated that the effectiveness of adaptive QWNNM models outperformed the original QWNNM model and other state-of-the-art satellite image restoration models in very different technique approaches.

**Keywords:** satellite images; image restoration and enhancement; adaptive noise-resilient block matching; adaptive feedback of residual images; adaptive iteration stopping criterion



**Citation:** Xu, X.; Zhang, Z.; Crabbe, M.J.C. Satellite Image Restoration via an Adaptive QWNNM Model. *Remote Sens.* **2024**, *16*, 4152. <https://doi.org/10.3390/rs16224152>

Academic Editors: Eugene Levin, Roman Shults and Surya Prakash Tiwari

Received: 30 September 2024

Revised: 1 November 2024

Accepted: 6 November 2024

Published: 7 November 2024



**Copyright:** © 2024 by the authors. Licensee MDPI, Basel, Switzerland. This article is an open access article distributed under the terms and conditions of the Creative Commons Attribution (CC BY) license (<https://creativecommons.org/licenses/by/4.0/>).

## 1. Introduction

Hundreds of imaging satellites are orbiting the earth, and every day they beam vast oceans of information to databases on the ground. Satellite images, captured by various satellite platforms equipped with different types of sensors, have become invaluable large-scale resources for the observation of Earth's surface, possibly in a (near) real-time manner. They can provide powerful insights in monitoring environmental changes, supporting suitable urban planning and natural resource management, and ultimately helping to achieve United Nations Sustainable Development Goals. However, these satellite images are always distorted and degraded due to channel noise and random atmospheric turbulence. Therefore, the retrieved images require restoration to satisfy the need for appropriate visual quality before use in different applications. The whole process of satellite image restoration uses prior knowledge of degradation to recover an image's original quality. However, restoring images can be challenging due to information loss in degraded images, so it is necessary to search for an optimal compromise among noise elimination, distortion correction, and maintaining true image contents.

Low complexity and repetitive patterns in satellite images make the combination of similar patches in these images generate a low-rank matrix in mathematics, so the low-rank matrix approximation (LRMA) approach, which recovers the underlying low rank matrix from its degraded observation, has been used in image restoration and enhancement [1–3]. Direct minimization of matrix rank is a challenging duty in mathematics, so Candès and Recht [4] introduced a nuclear norm of matrices as a convex surrogate for such a minimization. Candès and Tao [5] further showed that nuclear norm minimization (NNM) is the optimal convex approximation for matrix rank. The NNM can efficiently implement the minimization by using various algorithms like singular value thresholding [6]. However,

when viewing satellite image patches as matrices, the larger singular values are always more important than the smaller ones since they represent the energy of major structures and textures in satellite images. Since the NNM model overlooks differences among singular values, leading to the loss of important information, Gu et al. [7] proposed the matrix weighted nuclear norm (WNNN) model, where weights decrease as singular values increase, allowing for better handling of image features such as edges and textures. This results in improved noise and blur removal while preserving important details, enhancing the overall quality of restored images.

For the issue of multi-channel satellite image restoration, in order to overcome suboptimal results that may arise from independently processing different channels [8], strategies such as color space conversion or multi-channel joint processing can be employed to optimize the multi-channel satellite image processing workflow. The well-known block-matching and 3D filtering (CBM3D) model [9] first projects the sRGB color space to a luminance–chrominance space and then applies BM3D to each channel separately. The use of quaternion representation to encode image channels is another approach to preserving the interrelationships among color channels. Carmelil & Turek [10] and Xu et al. [11] proposed the generalized quaternion singular value decomposition K-means clustering (K-QSVD) in image presentation. Wang et al. [12] and Jia et al. [13] used the quaternion non-local means (QNLN) model, which integrates quaternion theory with non-local means (NL-means) filtering, to denoise satellite images. Yu et al. [14] extended the weighted nuclear norm minimization (WNNM) model to the quaternion domain, introducing the quaternion-based weighted nuclear norm minimization (QWNNM) model for color image denoising. Huang et al. [15,16] further advanced the QWNNM model by representing the 2D blur matrix in the quaternion domain and introducing a corresponding quaternion blur operator. Additionally, quaternion-based representation can restore missing data in color images [17], detect salient regions [18], facilitate facial recognition classification [19], perform color image deblurring [20], smooth and segment color images [21], and denoise images [22,23].

The known QWNNM model for satellite image restoration has notable limitations. Firstly, while it employs block matching to group image patches with similar features in degraded images, it does not account for potential noise interference. This oversight can introduce bias into the matching results, ultimately affecting the accuracy of subsequent processing tasks. Next, the residual image, which represents the pixel-wise difference between the original and restored images, contains valuable information for analyzing image quality. The QWNNM model lacks an effective feedback mechanism for utilizing such information during its iterative process and then limits its ability to optimize restoration results. Finally, due to the inherent diversity of land use, the number of iterations required for optimal restoration varies. However, the QWNNM model adopts a fixed iteration number, which may lead to suboptimal or over-restoration outcomes.

To address these drawback issues in the original QWNNM model, in this study, we designed three brand-new adaptive strategies: (a) *Adaptive Noise-Resilient Block Matching*: quaternion DCT is used to convert each satellite image patch from the quaternion domain to the frequency domain, and then quaternion soft thresholding is used to shrink the frequency coefficients for initial denoising. After that, block matching is then performed using these truncated frequency coefficients. This strategy to measure the similarity in the frequency domain after soft thresholding can mitigate the impact of noise on block similarity measurements. (b) *Adaptive Feedback of Residual Images*: An adaptive proportion of the residual satellite image is incorporated into the input satellite image for the subsequent iteration. This feedback mechanism enables our improvement to dynamically adjust its restoration strategy by utilizing useful information in the residual image, finally enhancing restoration performance. (c) *Adaptive Iteration Stopping Criterion*: A stopping criterion during the iterative process is proposed, which utilizes the specific characteristics of the image being restored, ensuring that the iteration halts at the optimal iteration number for each image.

Our proposed multi-strategy solution comprehensively addresses the limitations of the original QWNNM model, thereby enhancing performance, robustness, and adaptability in satellite image restoration and enhancement. Experimental results on satellite images demonstrated that our proposed model outperformed the original QWNNM model and other state-of-the-art restoration models in very different technique approaches.

## 2. Related Work

The weighted nuclear norm minimization (WNNM) model was first proposed by Gu et al. [7] for grayscale image denoising. It uses non-local self-similarity to collect similar patches of a given reference patch to form a group. Various similarity tools, such as K-means clustering [24], self-organizing maps [25], fuzzy clustering [26], and vector quantization [27], can be applied for grouping. The design of the WNNM model only adopts a simple grouping technique known as matching, which is accomplished by pairwise calculating the Euclidean-distance based similarity between the reference patch and candidate patches located at different spatial locations. These similar image patches can form a matrix with low rank, so the use of low-rank matrix minimization algorithms in mathematics can recover a noise-free reference patch from similar noisy patches. However, it is a non-convex NP-hard problem [6,28].

The nuclear norm minimization (NNM) [6,28,29] model, as a convex relaxation of the low-rank matrix approximation problem, has garnered significant research interest in recent years. The nuclear norm of a matrix is defined as the sum of its singular values, i.e.,

$$\|\mathbf{D}\|_* = \sum_i |\sigma_i(\mathbf{D})| \quad (1)$$

where  $\sigma_i(\mathbf{D})$  is the  $i$ -th singular value of the matrix  $\mathbf{D}$ . The NNM problem can be described as

$$\hat{\mathbf{D}} = \underset{\mathbf{D}_j}{\operatorname{argmin}} \|\mathbf{R} - \mathbf{D}\|_F^2 + \lambda \|\mathbf{D}\|_* \quad (2)$$

where  $\mathbf{R}$  is the observation matrix and  $\lambda$  is a positive constant. Cai et al. [6] proved that the solution of the NNM problem can be estimated by using the soft thresholding operation on the singular values:

$$\hat{\mathbf{D}} = \mathbf{U} \mathbf{S}_\lambda(\Sigma) \mathbf{V}^T \quad (3)$$

where  $\mathbf{R} = \mathbf{U}\Sigma\mathbf{V}^T$  and  $\mathbf{S}_\lambda(\Sigma)$  is the soft thresholding operator on the diagonal matrix  $\Sigma$ .

Although the NNM model is the tightest convex relaxation of the non-convex low-rank matrix approximation problem through incorporating the data fidelity term, it regularizes each singular value equally to maintain the convexity of the objective function, which significantly limits its capability and flexibility. To overcome these limitations, Gu et al. [7] proposed the Weighted Nuclear Norm Minimization (WNNM) model, in which different weights are assigned to different singular values. The WNNM model adopts a weighted nuclear norm:

$$\|\mathbf{R}\|_{\mathbf{w},*} = \sum_i |w_i \sigma_i(\mathbf{R})|, \quad (4)$$

where  $\mathbf{w} = [w_1, w_2, \dots, w_n]$  and  $\sigma_i(\mathbf{R})$  is the  $i$ -th singular value of  $\mathbf{D}$ . And

$$\mathbf{S}_{\mathbf{w}}(\Sigma_{ii}) = \max(\Sigma_{ii} - w_i, 0) \quad (5)$$

where  $\Sigma_{ii}$  is the diagonal element of  $\Sigma$ . The denoising performance of the WNNM model demonstrated that it cannot only lead to visible PSNR improvements over state-of-the-art models such as BM3D but also preserve much better the image local structures and generate fewer visual artifacts [7].

In order to avoid the suboptimal results that may arise from independently processing different channels of images [8], it is feasible to use a pure quaternion matrix to represent multi-channel images:

$$\mathcal{D} = (d_{ij}) \in \mathbb{H}^{m \times n} \quad (6)$$

where each pixel within a multi-channel image is encoded as a quaternion  $d_{ij}$  [30]:

$$d_{ij} = d_{ij}^r \mathbf{i} + d_{ij}^s \mathbf{j} + d_{ij}^b \mathbf{k} \quad (7)$$

and  $\{\mathbf{i}, \mathbf{j}, \mathbf{k}\}$  constitutes three imaginary units of the quaternion algebra satisfying

$$\mathbf{i}^2 = \mathbf{j}^2 = \mathbf{k}^2 = \mathbf{ijk} = -1$$

$$\mathbf{ij} = \mathbf{k} = -\mathbf{ji}, \mathbf{jk} = \mathbf{i} = -\mathbf{kj}, \mathbf{ki} = \mathbf{j} = -\mathbf{ik}$$

The conjugate operator  $\mathcal{D}^*$ , the transpose operator  $\mathcal{D}^T$ , and the conjugate transpose operator  $\mathcal{D}^\Delta$  are defined as:

$$\mathcal{D}^* = (d_{ij}^* = d_{ij}^r \mathbf{i} - d_{ij}^s \mathbf{j} - d_{ij}^b \mathbf{k}), \mathcal{D}^T = (d_{ji}) \quad (8)$$

The Unitary Quaternion Matrix  $\mathcal{D} \in \mathbb{H}^{m \times m}$  is called a unitary quaternion matrix if

$$\mathcal{D}^\Delta \mathcal{D} = \mathcal{D} \mathcal{D}^\Delta = \mathcal{I}_m \quad (9)$$

where  $\mathcal{I}_m$  is the quaternion identity matrix. Chen et al. [31] established the quaternion singular value decomposition (QSVD): For any quaternion matrix  $\mathcal{Q} \in \mathbb{H}^{m \times n}$  of rank  $r$ , there exist two unitary quaternion matrices  $\mathcal{U} \in \mathbb{H}^{m \times m}$  and  $\mathcal{V} \in \mathbb{H}^{n \times n}$  such that

$$\mathcal{Q} = \mathcal{U} \begin{pmatrix} \Sigma & 0 \\ 0 & 0 \end{pmatrix} \mathcal{V}^*, \quad (10)$$

where  $\Sigma = \text{diag}(\sigma_1, \dots, \sigma_r) \in \mathbb{R}^{r \times r}$ , and all singular values  $\sigma_i > 0, i = 1, \dots, r$ .

Since the real-valued WNNM model often introduces color distortions and artifacts when used for color image denoising [7], Yu et al. [14] innovatively incorporated the quaternion representation of color images into the WNNM model. Such an integration leads to the development of the quaternion weighted nuclear norm minimization (QWNNM) model. Huang et al. [15] further expanded the application of the QWNNM model to tackle the challenge of color image deblurring problem:

$$\min_{\mathcal{D}} \frac{\lambda}{2} \|\mathcal{A}\mathcal{D} - \mathcal{R}\|_F^2 + \|\mathcal{D}\|_{\mathbf{w},*} \quad (11)$$

where  $\mathcal{D} \in \mathbb{H}^{m \times n}$  and  $\mathcal{R} \in \mathbb{H}^{m \times n}$  are the quaternion-encoded counterparts of clean and degraded color images, respectively,  $\mathcal{A} \in \mathbb{H}^{m \times n}$  is the quaternion-encoded blur matrix, and  $\|\cdot\|_{\mathbf{w},*}$  is the quaternion weighted nuclear norm:

$$\|\mathcal{D}\|_{\mathbf{w},*} = \sum_i |w_i \sigma_i(\mathcal{D})|, \quad (12)$$

where the weight  $w_i$  is set as:

$$w_i = c\sqrt{n} / (\sigma_i(\mathcal{D}) + \varepsilon)$$

$$\sigma_i(\mathcal{D}) = \sqrt{\max(\sigma_i^2(\mathcal{R}) - n\sigma_n^2, 0)} \quad (13)$$

where  $c > 0$  is a positive constant,  $n$  is the number of similar patches, and  $\varepsilon = 10^{-16}$  is a small positive number to prevent the denominator from being zero. By introducing

an auxiliary quaternion variable  $\mathcal{G}$  and Lagrange multiplier  $\mathcal{L} \in \mathbb{H}^{m \times n}$ , the augmented Lagrangian function of the color image deblurring problem can be formulated by

$$\mathcal{L}(\mathcal{D}, \mathcal{G}, \mathcal{L}) = \frac{\lambda}{2} \|\mathcal{A}\mathcal{D} - \mathcal{R}\|_F^2 + \|\mathcal{G}\|_{\mathbf{w},*} + \frac{\beta}{2} \|\mathcal{D} - \mathcal{G}\|_F^2 + \langle \mathcal{L}, \mathcal{D} - \mathcal{Z} \rangle \quad (14)$$

The quaternion alternating direction method of multipliers (QADMM) [15] is used to obtain the solver as follows:

$$\begin{cases} \mathcal{D}^{(k+1)} = \operatorname{argmin}_{\mathcal{D}} \mathcal{L}(\mathcal{D}, \mathcal{G}^{(k)}, \mathcal{L}^{(k)}), \\ \mathcal{G}^{(k+1)} = \operatorname{argmin}_{\mathcal{G}} \mathcal{L}(\mathcal{D}^{(k+1)}, \mathcal{G}, \mathcal{L}^{(k)}), \\ \mathcal{L}^{(k+1)} = \mathcal{L}^{(k)} + (\mathcal{D}^{(k)} - \mathcal{G}^{(k)}). \end{cases} \quad (15)$$

### 3. The Proposed Model: Adaptive QWNNM

The quaternion weighted nuclear norm minimization (QWNNM) model demonstrates superior restoration performance, but it has three significant drawbacks. First, its patch matching relies on noisy data, increasing the risk of mismatched patches. Second, it neglects the residual image—the difference between the original and the recovered image—by not considering it as feedback in each iteration. This omission results in missing fine details in the residual image that could enhance the quality of the restoration. Lastly, the number of iterations in the QWNNM model remains constant regardless of the image content and noise levels. To address these issues, we embedded three brand-new adaptive strategies into the QWNNM model and developed a new adaptive QWNNM for satellite image restoration and enhancement.

#### 3.1. Adaptive Noise-Resilient Block Matching

To reduce the impact of noise on the block matching process, this strategy transforms image patches from the traditional spatial domain to the quaternion frequency domain. Since noise and signal typically exhibit distinct characteristics in the frequency domain, we propose to apply a quaternion soft thresholding operation to shrink the frequency coefficients such that noise components can be effectively suppressed while preserving important image information. Block matching was then performed using the processed truncated frequency coefficients, improving the accuracy and robustness of the matching process.

Let  $\mathcal{P}_f$  be the  $f$ -th reference patch of size  $n \times n$  in a degraded image, and  $\mathcal{P}_i$  be the  $i$ -th candidate similar patch of  $\mathcal{P}_f$ . In the context of the QWNNM model, the process can be conceptualized as first engaging in image denoising during the initial step, followed by a concentration on image restoration in subsequent iterations. Consequently, during the phase of measuring similarity between image patches, we only consider the additive noise, i.e.,  $\mathcal{P}_f$  and  $\mathcal{P}_i$  can be written as:

$$\begin{cases} \mathcal{P}_f = \mathcal{P}_f^0 + \mathcal{N}_f^0 \\ \mathcal{P}_i = \mathcal{P}_i^0 + \mathcal{N}_i^0 \end{cases} \quad (16)$$

where  $\mathcal{P}_f^0$  and  $\mathcal{P}_i^0$  are the latent clean patches of  $\mathcal{P}_f$  and  $\mathcal{P}_i$  respectively.  $\mathcal{N}_f^0$  and  $\mathcal{N}_i^0$  are the noise with mean 0 and standard deviation  $\sigma$ . The expectation of the similarity  $\operatorname{Sim}(\mathcal{P}_f, \mathcal{P}_i)$  will be:

$$\begin{aligned} E\{\operatorname{Sim}(\mathcal{P}_f, \mathcal{P}_i)\} &= \frac{1}{n^2} E\left\{\left\|\mathcal{P}_f - \mathcal{P}_i\right\|_F^2\right\} = \frac{1}{n^2} E\left\{\left\|\left(\mathcal{P}_f^0 + \mathcal{N}_f^0\right) - \left(\mathcal{P}_i^0 + \mathcal{N}_i^0\right)\right\|_F^2\right\} \\ &= \frac{1}{n^2} E\left\{\left\|\left(\mathcal{P}_f^0 - \mathcal{P}_i^0\right) + \left(\mathcal{N}_f^0 - \mathcal{N}_i^0\right)\right\|_F^2\right\} \end{aligned} \quad (17)$$

Due to the fact that clean images and noise are uncorrelated, the above equation can be written as:

$$E\{\operatorname{Sim}(\mathcal{P}_f, \mathcal{P}_i)\} \approx \operatorname{Sim}(\mathcal{P}_f^0, \mathcal{P}_i^0) + \sigma^2 \quad (18)$$

This means that the similarity measure for degraded patches is a biased estimator of the similarity for clean patches, which increases the likelihood of incorrectly classifying dissimilar patches as similar.

Noticing that the majority of the energy in clear images is always concentrated in the top-left corner in the frequency domain while the energy in the degraded image is dispersed across the entire image plane due to the additive noise (e.g., Figure 1), we propose to perform a soft-thresholding operation on the quaternion-based frequency coefficients to effectively suppress noise and then minimize the bias in patch matching caused by noise.

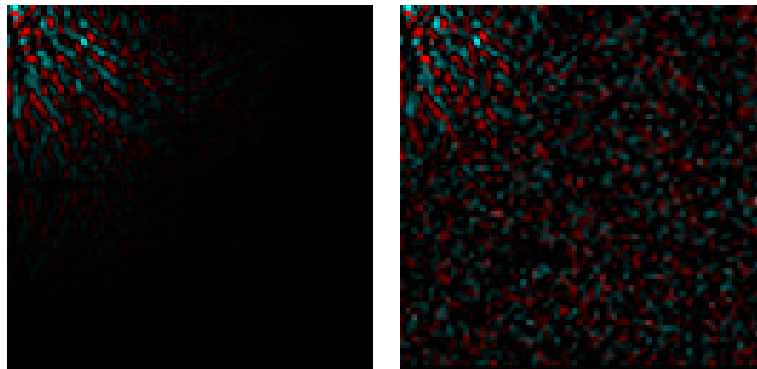


**Figure 1.** Magnitude of QDCT of clear and degraded images.

The soft thresholding operation is applied to the frequency domain of degraded patches  $\mathcal{P}_f$  and  $\mathcal{P}_i$ . Then the quaternion-DCT coefficient matrices after thresholding are

$$\begin{aligned} \mathcal{Z}_f &= \mathbf{D}_{\lambda_{QD}\sigma}(\mathbf{Q}_{QD}(\mathcal{P}_f)) \\ \mathcal{Z}_i &= \mathbf{D}_{\lambda_{QD}\sigma}(\mathbf{Q}_{QD}(\mathcal{P}_i)) \end{aligned} \quad (19)$$

where  $\mathbf{Q}_{QD}(\cdot)$  is a quaternion discrete cosine transform function,  $\lambda_{QD}$  is a fixed quaternion threshold parameter, and  $\mathbf{D}_\tau(\mathbf{x})$  is a soft-thresholding operator defined by:

$$\mathbf{D}_\tau(\mathbf{x}) \equiv \text{sgn}(\mathbf{x}) \max\{\mathbf{x} - \tau, 0\} \quad (20)$$

where  $\tau$  is a threshold, and the sign function  $\text{sgn}(\mathbf{x})$  of quaternion is defined as

$$\text{sgn}(\mathbf{x}) = \begin{cases} \frac{x_1}{|\mathbf{x}|} \mathbf{i} + \frac{x_2}{|\mathbf{x}|} \mathbf{j} + \frac{x_3}{|\mathbf{x}|} \mathbf{k}, & |\mathbf{x}| \neq 0 \\ 0, & |\mathbf{x}| = 0 \end{cases} \quad (21)$$

and  $x_1, x_2, x_3$  are three components of  $\mathbf{x}$ , respectively. The sign function for quaternions aligns with how the visual system perceives salient objects in an image [32,33], and it also helps in removing background clutter.

Finally, the similarity between degraded image patches can be defined as

$$\text{Sim}_{QD}(\mathcal{P}_f, \mathcal{P}_i) = \frac{\|\mathcal{Z}_f - \mathcal{Z}_i\|_F^2}{n^2} \quad (22)$$

### 3.2. Adaptive Feedback of Residual Images

The residual image, which represents the pixel-wise difference between the original and restored images, contains valuable information for analyzing image quality. The QWNNM model lacks an effective feedback mechanism for utilizing such information during its iterative process and then limits its ability to optimize restoration results. Therefore, we propose to use a portion of the residual image generated in the current iteration as

feedback and incorporate it into the input image for the next iteration. This feedback mechanism allows the restoration model to continuously learn and adjust during the iterative process, making better use of the useful information contained in the residual image to optimize the denoising results. By gradually approximating the true noise-free image, this approach enhances the overall denoising performance.

Let  $\mathcal{R}$  be a degraded image and  $\mathcal{J}$  be a simple restored operator. The restored image  $\hat{\mathcal{D}}$  can be written as  $\hat{\mathcal{D}} = \mathcal{J}(\mathcal{R})$  and the corresponding residual image is

$$\Delta\mathcal{D} = \mathcal{R} - \hat{\mathcal{D}} \quad (23)$$

The image restoration performance can be evaluated by a residual image. The fewer visible image structures in the residual image, the better the restoration performance. Even the most advanced restoration models still contain some image content in the residual image (e.g., Figure 2). To avoid information loss, an effective technique is to add the residual image back to the next filtered version, using it as feedback information and incorporating it into the input image for the subsequent iteration. This approach allows the restoration model to continuously learn and adjust during the iteration process, better utilizing the useful information in the residual image to optimize the restoration effect and gradually approach the true noiseless image. This can be formulated as:

$$\mathcal{R}^{(k+1)} = \hat{\mathcal{D}}^{(k)} + \delta_{(\sigma)}\Delta\mathcal{D}^{(k)} \quad (24)$$

where  $\hat{\mathcal{D}}^{(k)}$  is the  $k$ th reconstructed result,  $\Delta\mathcal{D}^{(k)} = \mathcal{R} - \hat{\mathcal{D}}^{(k)}$  is the  $k$ th residual image,  $\mathcal{R}^{(k+1)}$  is the next filtered version, and  $\delta_{(\sigma)}$  is the scale factor subject to the standard deviation  $\sigma$  of noise, a bigger feedback parameter  $\delta$  should be applied to images with strong noise content. Only one iterative operation of restoration cannot effectively remove the noise, while multiple iterations can achieve good performance. Therefore, our entire iterative process is

$$\begin{cases} \hat{\mathcal{D}}^{(k)} = \underset{X_j}{\operatorname{argmin}} \frac{\lambda}{2} \left\| \mathcal{R}^{(k)} - \mathcal{A}\mathcal{D}^{(k)} \right\|_F^2 + \left\| \mathcal{D}^{(k)} \right\|_{w,*} \\ \mathcal{R}^{(k+1)} = \hat{\mathcal{D}}^{(k)} + \delta_{(\sigma)}\Delta\mathcal{D}^{(k)} \end{cases} \quad (25)$$

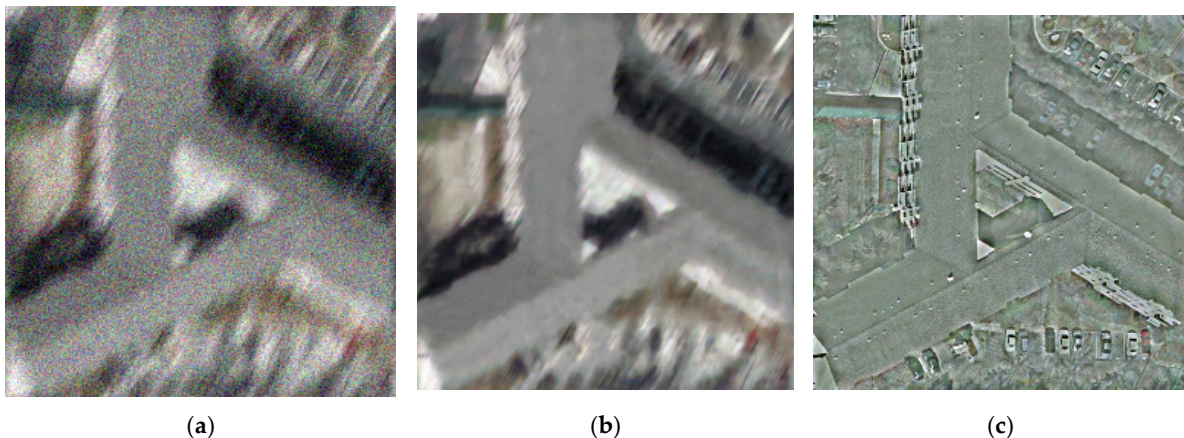


**Figure 2.** (a) Degraded image ( $\sigma = 25/\text{MB}(20, 60)$ ), (b) Restored image ( $\text{MB}(20, 60)/\sigma = 25$ ), (c) Residual image.

### 3.3. Adaptive Iteration Stopping Criterion

The original QWNNM model adopts an iterative process but uses a fixed number of iterations for all degraded images. However, as depicted in Figure 3, the quality of image restoration measured by PSNR/SSIM values varies with the number of iterations. Moreover, even for the same image, different noise levels require different iteration counts to achieve

the maximum PSNR/SSIM value. Since it is crucial to determine the optimal number of iterations required, we propose a stopping criterion to achieve the best restoration result. By precisely controlling the iterative process, the restoration model can achieve optimal restoration performance for different image contents, thereby enhancing the flexibility and practicality of the restoration algorithm.

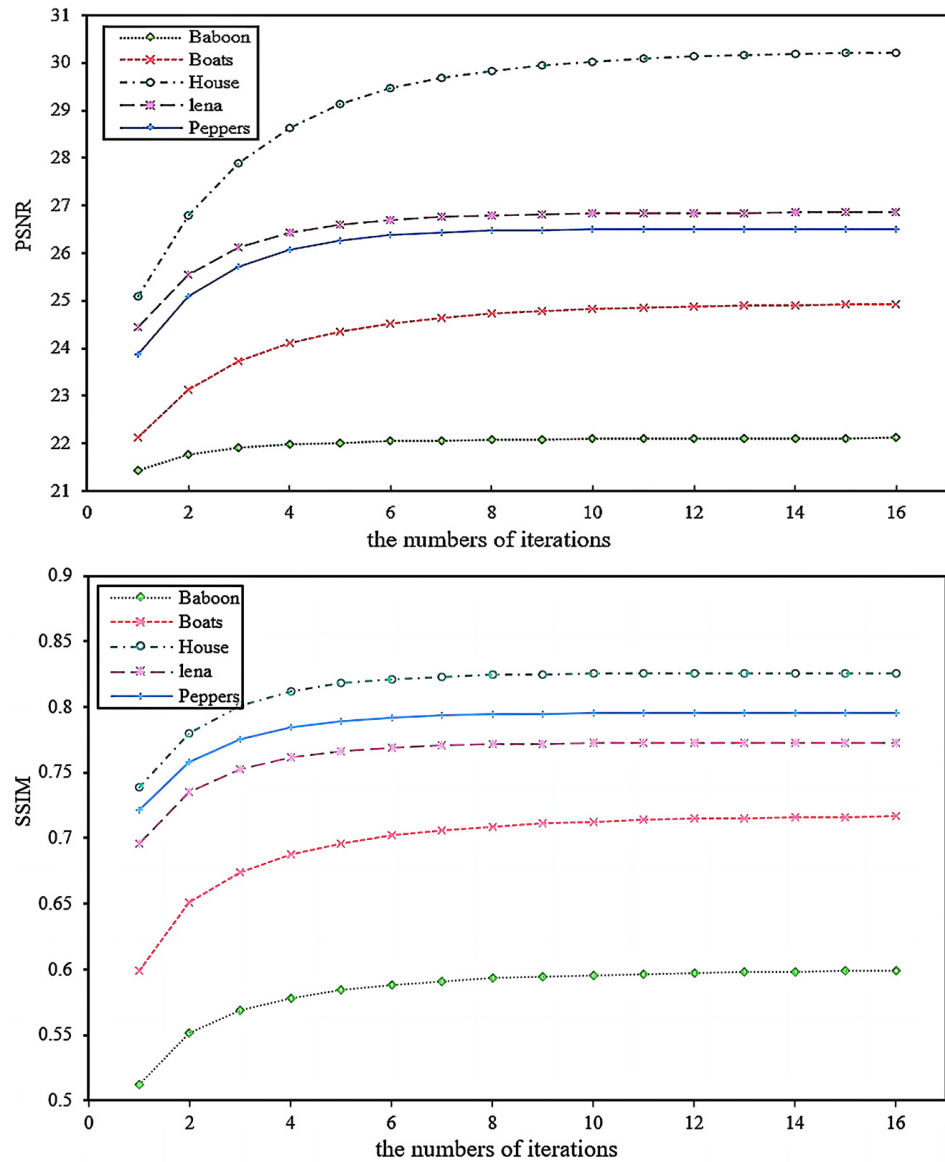


**Figure 3.** The quality of image restoration measured by PSNR/SSIM varies with the numbers of iterations.

The original image  $\mathcal{D}$ , and the additive noise  $\mathcal{N}$  are independent, and therefore we can assume that the less the dependency between the reconstructed  $\hat{\mathcal{D}}$  and method-noise image  $\Delta\mathcal{D} = \mathcal{R} - \hat{\mathcal{D}}$ , the better the restoration performance. Therefore, during the iteration process, we apply quaternion-based Pearson's correlation coefficient to measure the correlation of active regions in reconstructed and residual images.

$$\text{correl}(k) = \text{corr}\left(H * \hat{\mathcal{D}}^{(k)}, H * \left(\mathcal{R} - \hat{\mathcal{D}}^{(k)}\right)\right) \quad (26)$$

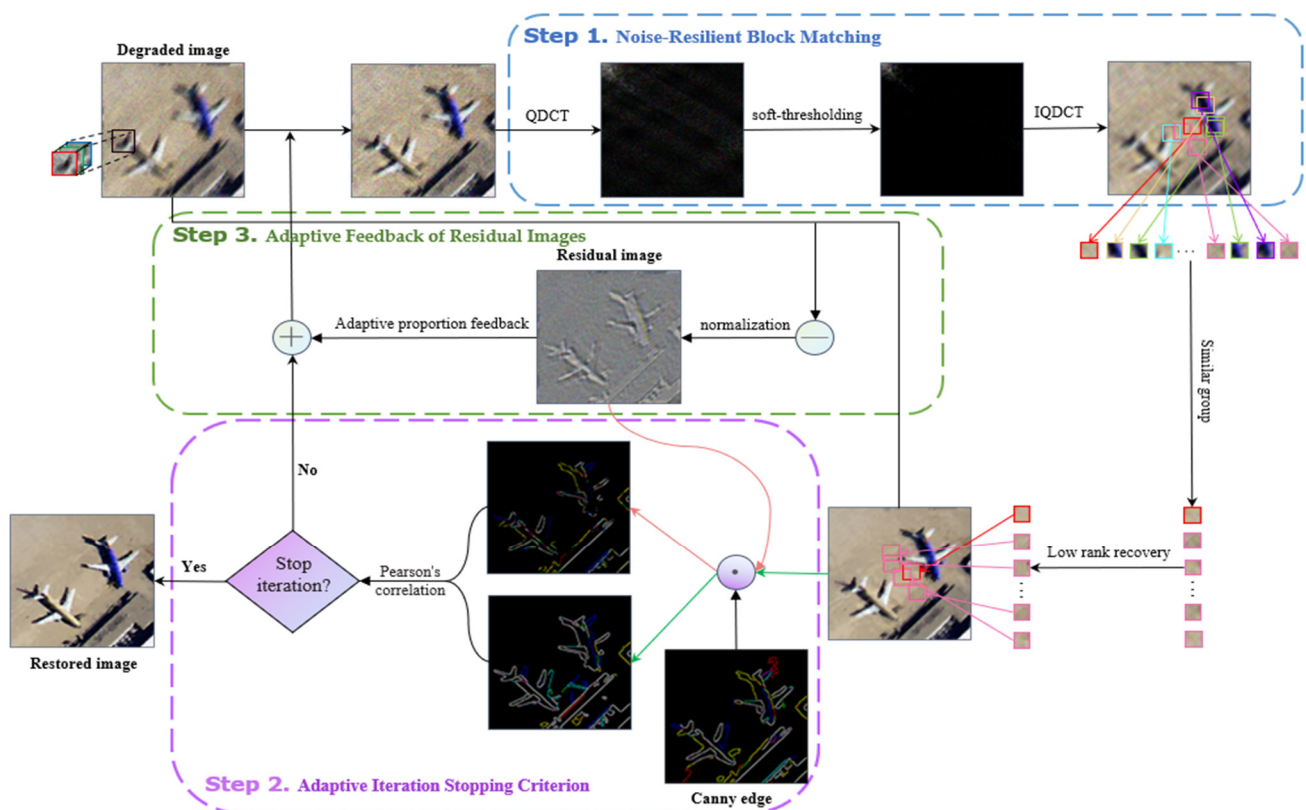
where  $H$  is a quaternion matrix obtained by dilating the result of the Canny edge detector [34] on  $\hat{\mathcal{D}}^{(1)}$  and indicates the active regions of an image, and  $\hat{\mathcal{D}}^{(k)}$  is the reconstructed



image after  $k$  iterations. The best iteration is the one that hits the minimum absolute value in the 'correl' vector, which is used as our stopping criterion.

### 3.4. Flowchat and Pseudocode

We embedded three brand-new adaptive strategies in Sections 3.1–3.3 into the original QWNNM and then developed the adaptive QWNNM model (see Algorithm 1). Figure 4 illustrates the flowchart of the framework of our adaptive QWNNM model. The input degraded satellite image is represented using quaternions, and the initial restoration result is transformed into the frequency domain by using Quaternion DCT (QDCT). Subsequently, the filtered image is obtained through the combination of the soft shrinkage threshold operation and the inverse Quaternion DCT (IQDCT). After that, it processes all patches within a predefined search window for a specific patch, grouping similar patches into a low-rank quaternion matrix. A low-rank recovery operation is performed on this array to reconstruct the key patch. Finally, it evaluates whether the correlation between the reconstructed image and the noise image has reached an extremum point. If this is not the case, a portion of the residual image will be adaptively fed back into the next iteration, continuing until the extreme point is achieved. For computational complexity in our adaptive QWNNM, the incorporation of the Iteration Stopping Criterion significantly reduces the number of iterations in the original QWNNM, while newly added Adaptive Noise-Resilient Block Matching and Feedback of Residual Images have low computational complexity, so our adaptive QWNNM has the similar computational complex as the original QWNNM.



**Figure 4.** The flowchart of the adaptive QWNNM model.

A pseudocode description of the entire adaptive QWNNM algorithm is as follows:

**Algorithm 1** Image Restoration with Adaptive QWNNM

---

**Input:**  
degraded image  $\mathcal{R}$ ; Initialize  $\mathcal{R}^{(0)} = \mathcal{R}$ ,  $\mathcal{D}^{(0)} = \mathcal{R}$ ,  $\mathcal{G}^{(0)} = \mathcal{D}^{(0)}$ ,  $\mathcal{L}^{(0)} = 0$ ;  
Set parameters  $\lambda, \beta$  and  $\rho$ ;

**Output:**  
The recovered image  $\hat{\mathcal{G}}^{(k)}$ ;

- 1: Estimate noise level  $\sigma$  (if necessary);
- 2: Map  $\delta_{(\sigma)}$  according to  $\sigma$ ;
- 3: **for**  $t = 1$ : kMax **do**
- 4:     Iterative regularization  $\mathcal{R}^{(k+1)} = \hat{\mathcal{G}}^{(k)} + \delta_{(\sigma)} \Delta \mathcal{G}^{(k)}$ ;
- 5:     Calculate  $\hat{\mathcal{D}}^{(k+1)}$ ;
- 6:     **for** each patch  $\mathcal{P}_i$  of  $\mathcal{E}^{(k+1)} = \hat{\mathcal{D}}^{(k+1)} + \frac{\mathcal{L}^{(k)}}{\beta}$  **do**
- 7:         Prefiltering for each degraded patch;
- 8:         Form a similar patch group  $\mathcal{E}_j$ ;
- 9:         Estimate weight vector  $w$ ;
- 10:         Quaternion singular value decomposition (QSVD)  $[\mathcal{U}, \Sigma, \mathcal{V}] = QSVD(\mathcal{E}_j)$ ;
- 11:         Get the patch estimation  $\hat{\mathcal{G}}_j$  using  $\mathcal{U} \Delta \mathcal{V}^*$ .
- 12:     **end for**
- 13:     aggregate all  $\hat{\mathcal{G}}_j$  together and get the restoration version  $\hat{\mathcal{G}}^{(k)}$ ;
- 14:     Update  $\mathcal{L}^{(k+1)} = \mathcal{L}^{(k)} + \rho (\hat{\mathcal{D}}^{(k)} - \hat{\mathcal{G}}^{(k)})$ .
- 15:     **if**  $t == 1$
- 16:         Compute  $H$
- 17:     **end if**
- 18:     Compute  $correl(t) = corr(H * \hat{\mathcal{G}}^{(k)}, H * (\mathcal{R} - \hat{\mathcal{G}}^{(k)}))$ ;
- 19:     **if**  $correl(t) > correl(t + 1)$
- 20:         break;
- 21:     **end if**
- 22: **end for**
- 23: **Return** The recovered image  $\hat{\mathcal{G}}^{(k)}$

---

**4. Satellite Image Restoration Experiments**

This section presents extensive experiments demonstrating the effectiveness of our proposed adaptive QWNNM model through the representative task of satellite image restoration. Our model was compared with image restoration models in very different technique approaches, including a fast-adaptive bilateral filter (F-ABF) [35] in a filtering technique, decorrelated vectorial total variation (DVTV) [36] in a regularization technique, and quaternions singular value decomposition K-means clustering (K-QSVD) [10,11] in sparse dictionary representation technique, block-matching and 3D filtering (BM3D) [37] and quaternion non-local means (QNLN) [12,13] in a nonlocal self-similarity prior technique, and quaternion non-local weighted nuclear norm minimization (QWNNM) [15] in a low-rank minimization technique.

Due to shaking and orientation tilting of satellite sensors, the obtained satellite images are always degraded by such motion blur. At the same time, noises in satellite images often originate from multiple sources, and the Central Limit Theorem in statistics demonstrates that the superposition of these noises can be approximated well by a Gaussian noise [38]. Moreover, Gaussian noise produces the largest degradation in satellite transmission systems since it possesses the greatest entropy and then the largest uncertainty [39,40]. Therefore, in simulation experiments, we used the combination of Gaussian noise and motion blur to simulate the noise/distortion existing in satellite images. At the same time, we conducted restoration experiments degraded by unknown haze, stripes, blurring, and so on in a real environment.

The known UC Merced Land Use dataset was manually extracted from large satellite images in the USGS National Map Urban Area Imagery series, and it includes 21 land use classes [41]. We randomly selected 1–3 images from each class and then obtained 51 test

satellite images (Figure 5). These test satellite images were subjected to a combination of “motion” type blurring and additive Gaussian noise, simulating real-world remote sensing observation conditions. We generated the blur kernels using the MATLAB command “fspecial”. In MATLAB, the command fspecial (‘motion’, LEN, THETA) returns a filter that, when convolved with an image, approximates linear motion of a camera by LEN pixels at an angle of THETA degrees counter patch wise. For horizontal and vertical motion, the filter becomes a vector. All the satellite image restoration experiments were implemented in MATLAB R2020a on a laptop with a 2.40 GHz Intel Core i5-1135G7 CPU and 8 GB @ 3200 MHz DDR4 memory.



**Figure 5.** All satellite images used in the restoration experiments, enumerated from left-to-right and top-to-bottom.

#### 4.1. Parameter Setting

These experiments were performed on simulated satellite image deblurring using a motion blur kernel with a length of 20 and an angle of 60, followed by the addition of additive Gaussian noise with ( $\sigma = 25$ ). All simulation experiments employ Peak Signal-to-Noise Ratio (PSNR) [42], Structural Similarity Index (SSIM) [43], Feature Similarity (FSIM) [44], and Erreur Relative Globale Adimension nelle de Synthèse (ERGAS) [45] as quantitative indicators of image restoration quality. For the restoration experiments in real environment, since without ground-truth image as reference, we used the no-reference evaluation indices: blind image integrity notator using DCT Statistics-II (BLIINDS 2) [46], blind/reference-less image spatial quality evaluator (BRISQUE) [47], and naturalness image quality evaluator (NIQE) [48].

PSNR and SSIM are commonly employed as the metrics in image restoration tasks: PSNR measures the similarity between the ground truth and the restored image based on Mean Squared Error (MSE), while SSIM assesses structural consistency. Unlike SSIM, FSIM aligns more closely with human visual perception by utilizing phase congruency and image gradient magnitude. ERGAS, which evaluates the quality of remote sensing image processing, considers the dimensional global error between the restored image and the reference image:

$$\text{ERGAS} = 100 \sqrt{\frac{1}{B} \sum_{b=1}^B \left( \frac{\text{MSE}_b}{M_b} \right)^2}, \quad (27)$$

where  $B$  represents the number of channels in satellite images,  $\text{MSE}_b$  is the  $b$ -th band MSE between predicted and reference images, and  $M_b$  is the average intensity of the  $b$ -th band of the reference. Higher PSNR, SSIM, and FSIM values indicate better restoration results, while a lower ERGAS value signifies a smaller difference between the restored image and the reference image, indicating higher quality.

The BLIINDS 2 [46] index is based on natural scene statistics (NSS) and assesses image quality in the DCT domain. It extracts features from the statistical properties of DCT coefficients and builds a predictive model from these features, enabling no-reference evaluation of image quality. This index highlights the role of NSS in quantifying perceptual quality in images. The BRISQUE [47] constitutes a no-reference index for assessing image quality, wherein spatial quality is quantified without reliance on a reference image. BRISQUE mea-

sures the perceived quality of images, with a lower value indicative of higher image quality. The NIQE [48] is a no-reference image quality assessment index designed to evaluate image quality. It uses NSS to extract features from images and fit them to a multivariate Gaussian model (MVG). Quality is assessed by measuring the distance between the image's feature parameters and those of the established model. Higher BLIINDS 2 values indicate better restoration results, while lower BRISQUE and NIQE values signify higher quality in the reconstructed images.

The parameters in our proposed model and the original QMNNM model were set as follows:  $\lambda = 115$ ,  $\beta = 7.5$ , the search window size was 30, the number of similar patches was 155, and the patch size was  $6 \times 6$ . The parameter  $\mu$  was set to 1.001 to ensure effective convergence. In order to choose the optimal values for  $\varepsilon$  and  $c$  in the weighting function, we investigated the PSNR and SSIM values for different  $\varepsilon$  and  $c$  during the restoration of satellite image 'Img47' (Figure 6). Clearly, the optimal value is  $c = 1.7 * \sqrt{2}$ . Since  $\varepsilon$  is defined as a small positive constant and the value of  $\varepsilon$  does not significantly affect the restoration results (Figure 6), we may set  $\varepsilon$  as the MATLAB built-in function 'eps' ( $=10^{-11}$ ). All comparison models were implemented using available code and default parameters from the corresponding papers [10–13,15,26–28].

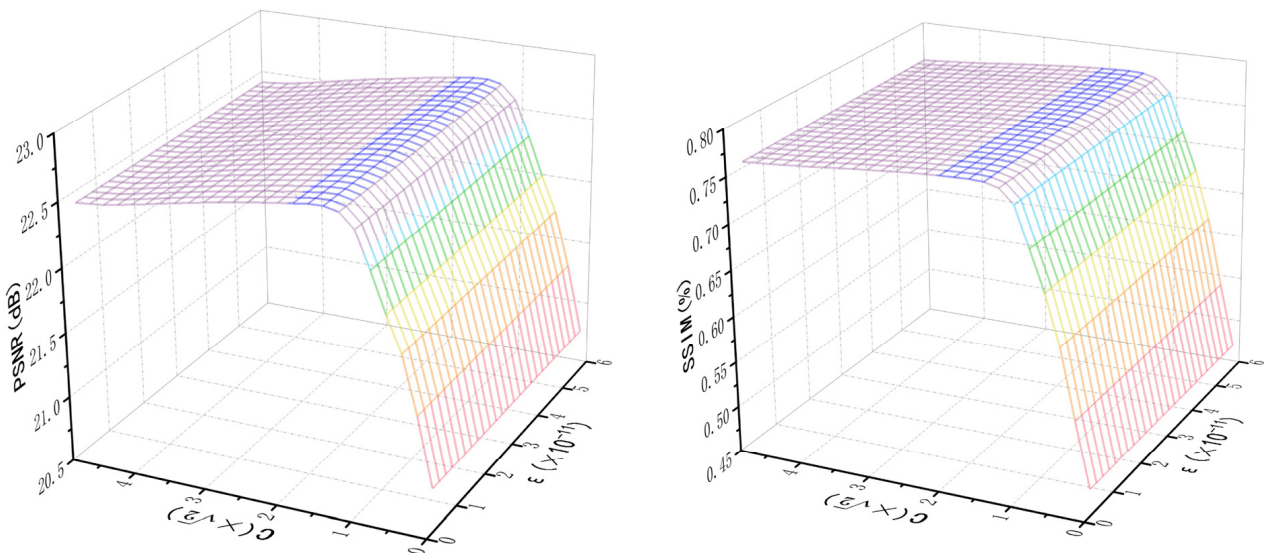


**Figure 6.** Evolution of PSNR (left) and SSIM (right) values for different parameters  $\varepsilon$  and  $c$  during the restoration of satellite image 'Img47'.

#### 4.2. Restoration Results

The PSNR/SSIM and FSIM/ERGAS values for the proposed adaptive QWNNM model under motion blur  $MB(20, 60)/\sigma = 25$ , compared to mainstream restoration models (F-ABF, K-QSVD, DTVT, BM3D, QNLM, and QWNNM), are presented in Tables 1 and 2. The best results are highlighted in bold. Figure 7 illustrates the average results. It is clear that our proposed model achieved superior restoration performance under motion blur conditions. In terms of PSNR/SSIM (Table 1), our adaptive QWNNM model demonstrates significant improvements over the five mainstream algorithms (F-ABF, K-QSVD, DTVT, BM3D, and QNLM), with average gains of 7.056/0.5024, 5.119/0.2876, 4.650/0.2022, 2.749/0.1134, 3.057/0.1373, and 2.226/0.1213, respectively. Regarding FSIM results (Table 2), our adaptive QWNNM model also shows notable improvements with increments of 0.1562, 0.1187, 0.1826, 0.1391, 0.0749, and 0.1146, respectively. Moreover, in terms of ERGAS (Table 2), our adaptive QWNNM model achieves substantial reductions of 197.4, 111.2, 93.45, 48.33, 52.06, and 41.42 compared to the mainstream models, as lower ERGAS values indicate better image quality. Especially when compared to the most closely related QWNNM model, our improvement achieves notable average gains of 1.596/0.0759 in PSNR/SSIM and 0.0227 in

FSIM, as well as a reduction of 27.15 in ERGAS. The primary reason for these improvements lies in the introduction of the three adaptive strategies (adaptive noise-resilient block matching, adaptive feedback of residual image, and adaptive iteration stopping criterion), leading to a more accurate reconstruction of structural details in satellite images.

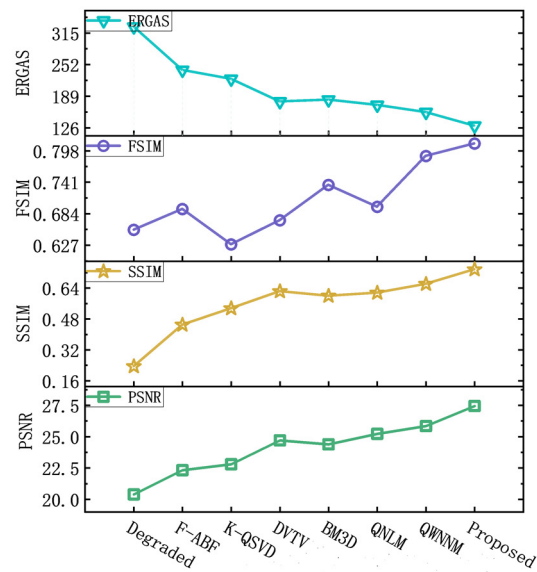
**Table 1.** PSNR (dB) and SSIM values of different restoration models for MB(20, 60)/ $\sigma = 25$  (the best result is in bold).

Image	Degraded	F-ABF [35]	K-QSVD [10,11]	DVTV [36]	BM3D [37]	QNLN [12,13]	QWNNM [15]	Proposed
1	23.70/0.2120	27.98/0.4936	29.21/0.6059	29.30/0.6089	28.86/0.5742	<b>30.16/0.6334</b>	29.01/0.5849	29.44/0.6246
2	17.58/0.2560	18.20/0.5042	18.44/0.6313	22.94/0.7901	22.90/0.7317	20.37/0.7106	26.09/0.8014	<b>29.38/0.8680</b>
3	21.44/0.2144	23.48/0.5085	24.05/0.6459	25.47/0.6896	25.52/0.6521	26.85/0.7318	26.73/0.6901	<b>29.03/0.7728</b>
4	22.76/0.2464	25.78/0.5293	26.53/0.6476	27.44/0.6755	26.95/0.6486	27.78/0.6698	27.60/0.6579	<b>28.13/0.7047</b>
5	21.85/0.2591	24.07/0.4678	24.33/0.5215	25.68/0.5794	25.39/0.5703	26.19/0.5856	25.98/0.6031	<b>26.76/0.6465</b>
6	16.48/0.1742	17.03/0.3135	17.13/0.3781	18.90/0.5170	18.57/0.4764	18.78/0.5005	20.10/0.5750	<b>21.95/0.6972</b>
7	15.74/0.2247	16.14/0.3386	16.24/0.3910	18.22/0.5472	17.51/0.4841	18.16/0.5145	19.43/0.6063	<b>21.86/0.7335</b>
8	20.50/0.2551	21.93/0.4585	22.37/0.5513	24.00/0.6178	23.96/0.6063	23.69/0.6145	25.53/0.6624	<b>27.08/0.7281</b>
9	20.66/0.2387	22.28/0.4443	22.50/0.5218	24.62/0.6129	24.87/0.6266	25.96/0.6833	26.26/0.6954	<b>28.21/0.7869</b>
10	18.51/0.2772	19.39/0.4336	19.57/0.4930	22.46/0.6326	21.97/0.6056	22.86/0.6443	23.61/0.6637	<b>25.72/0.7635</b>
11	18.47/0.2334	19.36/0.4055	19.48/0.4731	22.13/0.6119	21.86/0.5721	22.21/0.5868	23.55/0.6510	<b>25.64/0.7482</b>
12	19.96/0.2547	21.17/0.2766	20.85/0.1692	21.91/0.4116	23.39/0.6462	20.79/0.1458	25.31/0.7955	<b>26.39/0.8526</b>
13	17.61/0.2385	18.34/0.3559	18.45/0.3917	21.14/0.5604	20.94/0.5380	21.35/0.5304	22.92/0.6306	<b>25.16/0.7275</b>
14	19.94/0.2378	21.20/0.3724	21.33/0.3977	22.78/0.4887	22.40/0.4653	23.13/0.4759	23.35/0.5158	<b>24.35/0.5753</b>
15	18.98/0.2387	20.02/0.4031	20.20/0.4651	22.70/0.5754	22.38/0.5667	23.10/0.5888	24.24/0.6478	<b>25.86/0.7260</b>
16	21.10/0.2589	22.92/0.5305	23.26/0.6549	25.41/0.7417	26.02/0.7367	26.46/0.7638	28.09/0.7808	<b>30.30/0.8636</b>
17	17.03/0.2153	17.64/0.4022	17.77/0.5079	20.40/0.6738	19.65/0.5875	19.91/0.6182	21.64/0.7127	<b>23.65/0.8261</b>
18	15.78/0.1801	16.23/0.3364	16.32/0.4264	18.24/0.5886	18.00/0.5446	18.24/0.5534	19.99/0.6851	<b>22.38/0.8193</b>
19	23.67/0.2505	27.94/0.6485	29.25/0.8527	31.77/0.8786	30.64/0.8102	34.03/0.9055	32.45/0.8207	<b>34.09/0.8934</b>
20	23.78/0.2455	28.24/0.6307	29.69/0.8272	32.00/0.8570	31.36/0.7987	34.18/0.875	32.58/0.8071	<b>34.29/0.88985</b>
21	23.82/0.2409	28.34/0.6301	29.95/0.8276	32.75/0.8569	31.26/0.7879	32.42/0.797	<b>34.49/0.88230</b>	33.95/0.8645
22	20.78/0.1736	22.49/0.3324	22.91/0.3949	23.94/0.4361	24.30/0.4508	24.51/0.4504	25.64/0.5137	<b>26.74/0.5579</b>
23	22.20/0.2411	24.76/0.5248	25.26/0.6459	26.37/0.6743	26.57/0.6690	27.55/0.7026	27.72/0.6991	<b>29.08/0.7688</b>
24	18.47/0.1588	19.42/0.2908	19.71/0.3593	22.35/0.5281	22.64/0.5593	23.91/0.6261	24.72/0.6663	<b>27.50/0.7779</b>
25	22.15/0.2160	24.58/0.3454	24.89/0.3460	25.37/0.3917	25.20/0.4005	25.51/0.3938	<b>25.94/0.4228</b>	25.75/0.4300
26	21.77/0.2424	23.98/0.4178	24.17/0.4353	25.19/0.4995	25.10/0.5066	26.20/0.5173	25.81/0.5491	<b>26.44/0.5869</b>
27	22.07/0.2400	24.48/0.4116	24.75/0.4228	25.66/0.4874	25.40/0.4890	26.38/0.4895	25.98/0.5228	<b>26.58/0.5522</b>
28	20.50/0.2122	21.97/0.3018	22.07/0.2941	22.84/0.3817	22.62/0.3793	22.83/0.3289	23.13/0.4341	<b>23.60/0.4710</b>
29	19.59/0.3104	20.72/0.4886	20.94/0.5557	23.06/0.6670	22.90/0.6383	22.58/0.5916	24.45/0.7035	<b>26.06/0.7777</b>
30	19.92/0.2152	21.24/0.4039	21.44/0.4811	22.71/0.5567	22.63/0.5412	22.97/0.5572	23.61/0.5970	<b>24.87/0.6842</b>
31	18.46/0.2405	19.31/0.2986	19.33/0.2799	20.60/0.4391	20.48/0.4440	20.92/0.4025	22.02/0.5979	<b>23.83/0.7194</b>
32	19.81/0.2602	21.05/0.3796	21.06/0.3832	22.61/0.5342	22.32/0.5168	23.09/0.5184	24.19/0.6599	<b>25.89/0.7571</b>
33	20.37/0.2233	21.81/0.3454	21.88/0.3506	23.04/0.4590	22.64/0.4363	22.72/0.3793	23.97/0.5405	<b>25.06/0.6071</b>
34	18.98/0.2330	19.98/0.3970	20.18/0.4642	22.71/0.5802	22.22/0.5355	22.20/0.5261	23.67/0.6029	<b>24.82/0.6679</b>
35	20.87/0.2090	22.59/0.4518	22.92/0.5650	24.36/0.6201	24.53/0.6007	25.09/0.6269	26.26/0.6583	<b>28.18/0.7444</b>
36	16.04/0.1781	16.52/0.3003	16.61/0.3530	18.45/0.5008	18.01/0.4406	18.21/0.4373	19.67/0.5668	<b>22.28/0.7173</b>
37	18.48/0.2451	19.38/0.4272	19.56/0.5030	23.29/0.6612	22.99/0.6251	23.44/0.6437	25.18/0.6976	<b>27.36/0.7792</b>
38	23.69/0.2519	28.08/0.6556	29.89/0.8598	33.15/0.8731	31.06/0.8058	34.16/0.8823	33.13/0.8098	<b>34.66/0.8780</b>
39	24.01/0.2418	29.04/0.6595	31.63/0.8771	<b>36.43/0.8836</b>	32.20/0.8136	34.80/0.8978	33.76/0.8060	35.37/0.8786
40	21.85/0.2252	24.15/0.4756	24.76/0.5823	25.97/0.6291	25.45/0.5910	26.06/0.6168	26.26/0.6284	<b>26.88/0.6836</b>
41	23.15/0.2721	26.62/0.6028	27.28/0.7400	28.96/0.7718	28.56/0.7294	29.88/0.7863	29.33/0.7415	<b>30.43/0.7986</b>
42	24.14/0.2457	29.32/0.6184	31.10/0.7804	31.55/0.7920	30.82/0.7399	<b>33.30/0.8221</b>	31.35/0.7505	32.21/0.8058
43	22.96/0.2585	26.25/0.5904	27.14/0.7283	29.66/0.7684	29.04/0.7270	30.68/0.7794	30.19/0.7420	<b>31.38/0.7944</b>
44	20.96/0.2311	22.66/0.4541	23.01/0.5443	24.45/0.5946	24.01/0.5594	24.43/0.6027	25.32/0.5988	<b>26.52/0.6598</b>
45	14.53/0.1809	14.81/0.2854	14.94/0.3488	17.19/0.5218	16.62/0.4430	17.09/0.4499	18.92/0.5939	<b>22.10/0.7484</b>
46	20.26/0.2306	21.69/0.4963	21.93/0.6219	23.96/0.6849	23.97/0.6444	24.73/0.6968	25.92/0.7017	<b>27.93/0.7834</b>
47	20.23/0.2904	21.59/0.5131	21.89/0.6025	25.17/0.7029	24.48/0.6676	25.38/0.6998	26.62/0.7239	<b>28.46/0.7870</b>
48	20.29/0.2772	21.70/0.4866	21.98/0.5628	24.07/0.6459	23.94/0.6271	24.88/0.6576	25.30/0.6763	<b>26.99/0.7498</b>
49	22.50/0.2505	25.32/0.5472	25.98/0.6684	27.49/0.7057	27.37/0.6833	29.35/0.7585	28.80/0.7196	<b>29.98/0.7741</b>
50	22.80/0.2676	25.90/0.5941	26.54/0.7281	28.26/0.7666	28.12/0.7322	29.76/0.7938	29.30/0.7531	<b>30.71/0.8146</b>
51	18.34/0.1649	19.26/0.3177	19.58/0.3924	21.78/0.5091	22.95/0.5369	22.44/0.5115	25.46/0.6311	<b>28.29/0.7133</b>
Avg.	20.38/0.2341	22.32/0.4490	22.79/0.5344	24.69/0.6232	24.38/0.5993	25.21/0.6152	25.84/0.6607	<b>27.44/0.7366</b>

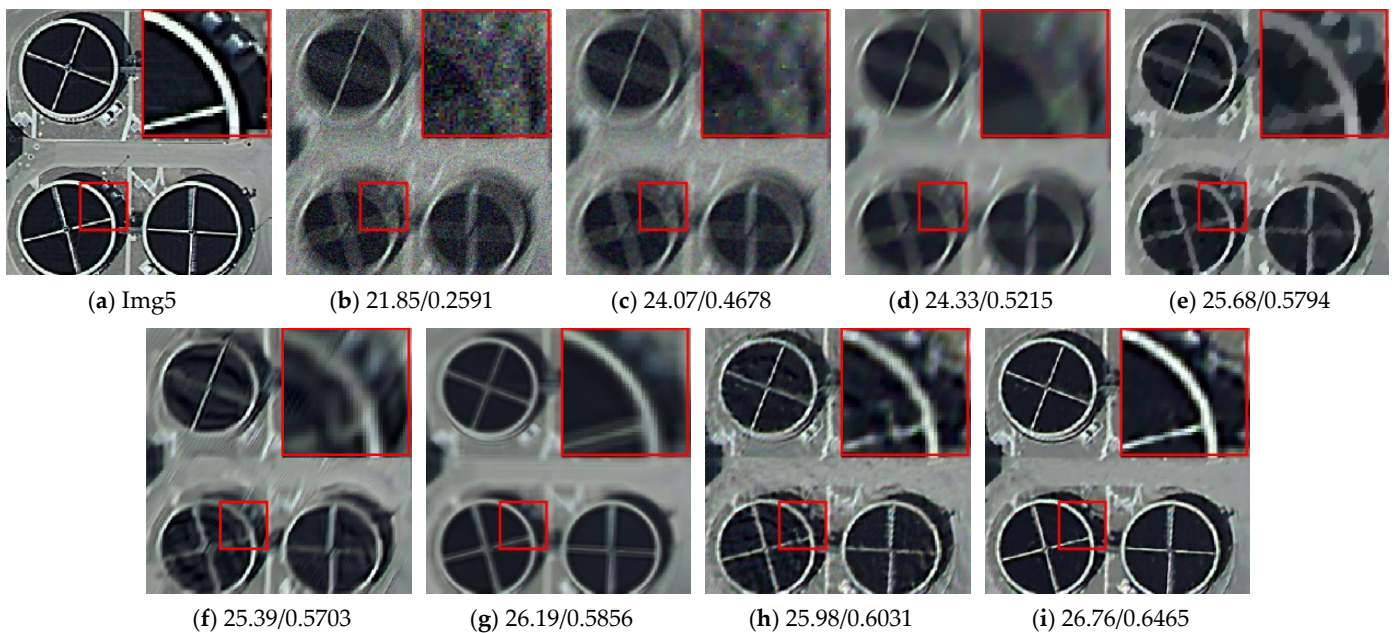
**Table 2.** FSIM and ERGAS values of different restoration models for MB(20, 60)/ $\sigma = 25$  (the best result is in bold).

Image	Degraded	F-ABF [35]	K-QSVD [10,11]	DVTV [36]	BM3D [37]	QNLN [12,13]	QWNNM [15]	Proposed
1	0.6995/258.5	<b>0.7296</b> /134.7	0.5639/102.1	0.5517/100.9	0.6726/104.3	0.5808/ <b>88.99</b>	0.7158/103.0	0.6491/99.37
2	0.5312/415.0	0.6067/356.1	0.6532/340.9	0.7754/204.1	0.7189/204.4	0.7168/273.5	0.8177/146.3	<b>0.8792/102.3</b>
3	0.6089/263.7	0.7147/177.9	0.6770/157.1	0.7146/134.0	0.7633/133.2	0.7705/114.2	0.7965/117.8	<b>0.8236/91.03</b>
4	0.7006/247.0	0.7336/145.3	0.6665/120.9	0.6661/107.2	0.7423/113.6	0.6981/102.5	<b>0.7691</b> /107.5	0.7556/ <b>100.5</b>
5	0.7406/295.5	0.7400/192.3	0.6154/174.6	0.6517/149.0	0.7418/153.2	0.6908/138.2	<b>0.7769</b> /147.6	0.7717/ <b>133.3</b>
6	0.6084/475.4	0.5991/417.9	0.5531/407.8	0.6118/333.6	0.6629/346.1	0.6299/338.0	0.7456/296.3	<b>0.7993/240.6</b>
7	0.6348/459.3	0.6541/414.4	0.6345/406.0	0.6755/325.0	0.7046/351.3	0.6877/325.8	0.7753/289.8	<b>0.8287/220.1</b>
8	0.6698/272.1	0.7143/199.9	0.6566/182.6	0.6700/151.5	0.7451/152.5	0.7057/157.5	0.7928/132.0	<b>0.8142/110.5</b>
9	0.6779/297.6	0.7254/212.9	0.6532/198.7	0.6793/155.5	0.7621/150.1	0.7566/131.2	0.8082/132.9	<b>0.8450/105.6</b>
10	0.6604/369.1	0.6843/301.5	0.6631/289.4	0.7095/205.8	0.7403/216.0	0.7386/193.8	0.7834/188.5	<b>0.8318/146.4</b>
11	0.5921/328.3	0.6368/270.0	0.6270/260.7	0.6765/192.6	0.6916/196.8	0.6746/188.8	0.7549/168.5	<b>0.8123/132.1</b>
12	0.7496/344.9	0.6143/264.4	0.3196/265.4	0.6345/234.0	0.7725/198.4	0.2755/265.7	0.8374/160.7	<b>0.8479/142.3</b>
13	0.6723/359.8	0.6573/304.8	0.5956/295.8	0.6487/216.7	0.7261/220.0	0.6907/208.9	0.7886/184.8	<b>0.8260/142.7</b>
14	0.6772/311.9	0.6756/237.1	0.5730/225.6	0.6321/191.1	0.6828/199.3	0.6494/183.3	0.7264/184.1	<b>0.7458/163.0</b>
15	0.6857/313.1	0.6927/248.8	0.6329/237.5	0.6606/177.4	0.7438/183.4	0.7157/167.2	0.7993/154.1	<b>0.8249/126.4</b>
16	0.6390/283.4	0.7046/201.5	0.7061/185.6	0.7098/146.2	0.7870/132.8	0.7696/126.6	0.8317/113.5	<b>0.8735/86.88</b>
17	0.5589/445.4	0.5827/386.4	0.6016/375.6	0.6765/277.2	0.6725/300.6	0.6712/291.5	0.7683/243.7	<b>0.8331/194.1</b>
18	0.5510/458.0	0.5357/411.0	0.5416/402.8	0.6008/322.0	0.6269/331.1	0.6175/321.9	0.7448/266.5	<b>0.8199/203.0</b>
19	0.5739/286.8	0.7712/151.4	0.8118/115.3	0.8273/88.25	0.8449/95.99	0.8649/ <b>66.15</b>	0.8707/81.46	<b>0.8940</b> /70.95
20	0.6067/251.0	0.7823/134.5	0.7999/103.4	0.8110/81.99	0.8560/80.52	0.8628/ <b>58.36</b>	0.8816/72.01	<b>0.8908</b> /62.62
21	0.6175/259.3	0.7884/137.3	0.7878/103.5	0.8071/75.58	0.8423/84.07	0.8459/75.11	0.8660/ <b>58.76</b>	<b>0.8675</b> /66.28
22	0.6710/265.4	0.6585/188.6	0.5328/171.6	0.5341/152.3	0.6766/147.1	0.6170/143.3	<b>0.7370</b> /128.6	0.7313/ <b>114.3</b>
23	0.6587/302.9	0.7253/190.3	0.6755/168.0	0.6813/148.1	0.7560/142.0	0.7342/125.7	0.7932/134.2	<b>0.8056/112.5</b>
24	0.6660/386.5	0.6540/313.3	0.5583/296.1	0.6257/219.2	0.7353/212.9	0.7272/184.3	0.7947/173.4	<b>0.8436/127.7</b>
25	0.7225/356.7	<b>0.7695</b> /223.7	0.4748/198.5	0.5380/187.9	0.6656/192.1	0.5660/ <b>176.4</b>	0.6927/187.2	0.6411/181.8
26	0.7450/383.2	0.7244/242.3	0.5466/217.9	0.5996/193.0	0.7111/196.9	<b>0.7471</b> /170.5	0.6456/184.6	0.7372/ <b>169.5</b>
27	0.7023/313.9	0.7286/198.4	0.5203/177.8	0.5922/159.8	<b>0.7533</b> /164.3	0.6206/145.9	0.7376/155.7	0.7195/ <b>144.5</b>
28	0.5217/339.0	0.6447/247.3	0.4316/233.9	0.5340/215.1	0.6366/220.7	<b>0.7279</b> /215.8	0.6863/210.6	0.6811/ <b>199.6</b>
29	0.6478/350.4	0.6827/272.4	0.6754/258.1	0.7038/201.2	0.7388/204.6	0.6915/211.0	0.7922/180.4	<b>0.8330/147.2</b>
30	0.6382/324.3	0.6638/247.8	0.6182/234.8	0.6452/202.1	0.7035/202.4	0.6780/194.1	0.7390/187.5	<b>0.7766/161.4</b>
31	0.7091/363.9	0.6478/299.9	0.5235/293.3	0.6039/252.5	0.6886/255.9	0.6124/243.3	0.7837/217.8	<b>0.8423/176.1</b>
32	0.6892/317.4	0.6745/242.6	0.5812/234.9	0.6525/195.1	0.7105/202.1	0.6763/184.5	0.8031/166.2	<b>0.8518/135.9</b>
33	0.6837/283.6	0.6261/210.3	0.4728/201.3	0.5704/176.8	0.6519/184.0	0.5466/181.2	0.7320/162.5	<b>0.7528/145.6</b>
34	0.6472/336.3	0.6659/268.9	0.6235/256.6	0.6607/191.8	0.7091/200.8	0.6769/200.2	0.7594/176.8	<b>0.7782/152.9</b>
35	0.6415/315.0	0.6761/223.9	0.6127/205.8	0.6316/175.1	0.7163/171.4	0.6759/161.0	0.7725/146.1	<b>0.8056/118.6</b>
36	0.5879/454.3	0.5864/404.6	0.5568/396.0	0.6010/319.7	0.6500/336.5	0.6243/328.7	0.7382/282.7	<b>0.8155/209.0</b>
37	0.6561/392.4	0.6809/320.0	0.6509/307.1	0.7093/200.3	0.7669/208.1	0.7497/197.7	0.8293/170.4	<b>0.8573/131.8</b>
38	0.5975/213.4	0.7751/109.5	0.8018/78.62	0.7885/51.41	0.8396/65.73	0.8211/ <b>44.99</b>	0.8754/51.37	<b>0.8890</b> /45.96
39	0.5751/209.3	0.7705/103.1	0.8093/70.06	0.8109/45.25	0.8362/59.50	0.8308/ <b>35.99</b>	0.8731/48.64	<b>0.8831</b> /43.96
40	0.6528/246.1	0.6844/162.0	0.6259/142.6	0.6630/122.8	0.7153/129.6	0.6929/120.9	0.7612/119.8	<b>0.7671/111.0</b>
41	0.6724/264.3	0.7890/151.2	0.7606/127.2	0.7676/105.3	0.8205/107.8	0.8036/93.47	0.8387/102.9	<b>0.8461/90.63</b>
42	0.6530/293.6	0.8111/139.1	0.7490/93.67	0.7453/87.41	0.8175/94.49	0.7953/ <b>70.94</b>	<b>0.8422</b> /88.65	0.8252/82.45
43	0.7034/288.6	0.8000/167.2	0.7350/137.5	0.7548/102.6	0.8245/109.0	0.7919/89.25	<b>0.8561</b> /101.1	0.8432/ <b>89.19</b>
44	0.6374/261.6	0.6797/187.8	0.6289/172.6	0.6672/146.3	0.7113/152.2	0.6933/144.6	0.7487/133.8	<b>0.7651/116.5</b>
45	0.5545/604.2	0.5614/559.4	0.5447/547.3	0.6287/422.4	0.6538/451.8	0.6463/429.4	0.7509/351.5	<b>0.8295/246.1</b>
46	0.6032/289.3	0.6811/214.2	0.6799/200.5	0.6934/159.2	0.7358/158.7	0.7271/145.3	0.7786/130.6	<b>0.8190/104.6</b>
47	0.7084/306.6	0.7454/229.9	0.6959/214.7	0.7261/148.2	0.7947/158.6	0.7733/143.3	0.8442/132.9	<b>0.8600/106.9</b>
48	0.6874/287.0	0.7163/212.7	0.6548/198.8	0.6915/155.4	0.7508/156.5	0.7387/138.8	0.7979/139.7	<b>0.8260/113.6</b>
49	0.6858/279.4	0.7656/172.7	0.6937/149.0	0.7081/124.3	0.7897/123.9	0.7773/97.98	0.8234/109.0	<b>0.8259/94.68</b>
50	0.6749/255.0	0.7793/151.3	0.7494/128.7	0.7505/106.0	0.8173/105.7	0.8040/87.65	0.8412/97.30	<b>0.8544/82.70</b>
51	0.6326/419.8	0.6338/347.8	0.5243/330.2	0.5898/256.8	0.7066/220.9	0.6339/234.5	0.7758/174.9	<b>0.8162/132.1</b>
Avg.	0.6546/327.4	0.6921/241.2	0.6283/223.4	0.6718/178.3	0.7359/182.0	0.6962/171.4	0.7882/157.1	<b>0.8109/130.0</b>

It is well established that human perception serves as the ultimate criterion for assessing image quality and plays a pivotal role in evaluating the performance of restoration algorithms. Figures 8–12 demonstrate the visual enhancements achieved by our proposed model and others. Not only did it display the overall image reconstructed by various models, but it also showed the image of the small red box area zoomed by about 2.5 times, providing a clearer and more intuitive reconstruction effect.



**Figure 7.** Four quantitative indicators for the average quality of satellite image restoration using different models.



**Figure 8.** Restoration performance on “Img5” with visual quality and numerical results (PSNR/SSIM). (a) Ground truth; (b) Degraded image with motion kernel (20, 60) and noise level  $\sigma = 25$ ; Restored satellite image by (c) F-ABF [35]; (d) K-QSVD [10,11]; (e) DTV [36]; (f) BM3D [37]; (g) QNLM [12,13]; (h) QWNNM [15]; (i) adaptive QWNNM (ours).

For the restoration of “Img5”, compared to seven mainstream models, it is evident that our proposed model significantly enhanced the visual quality of the tank image. This improvement was particularly pronounced in the enhancement of the tank edges and the blurred background, as illustrated in the zoomed-in satellite image within the red box. Traditional models like the F-ABF and K-QSVD models did not adequately account for the degradation caused by the motion blur kernel, resulting in excessive distortion of circular and rectangular structures. BM3D, DTV, and QNLM models struggled with noise removal, leading to the loss of critical details in both the tank and the background. Although the QWNNM model produced better visual results than the aforementioned models, it still tended to overly blur the image. In contrast, our adaptive QWNNM model successfully

preserved structural integrity and details, yielding clearer edges and an enhanced overall background. The edges of the tank, wires, and shadows were particularly pronounced in the zoomed-in image, highlighting our model's superior enhancement capability in achieving clearer and more visually satisfying results.

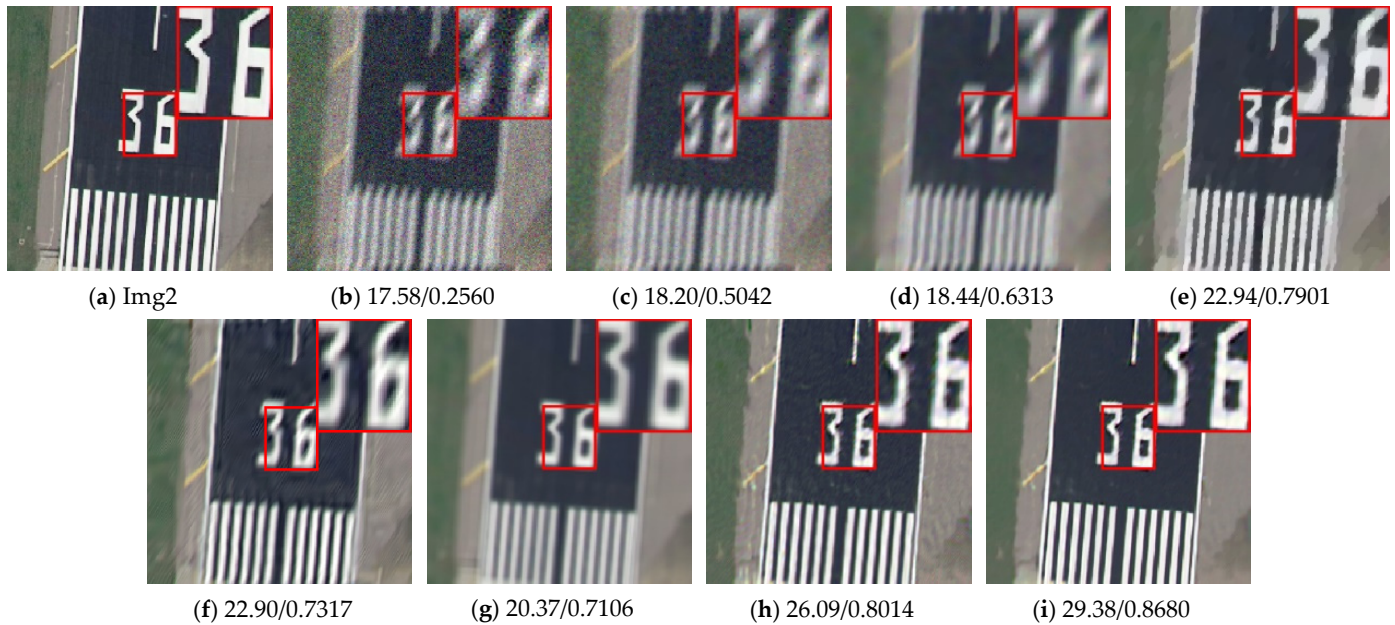


**Figure 9.** Restoration performance on “Img2” with visual quality and numerical results (PSNR/SSIM). (a) Ground truth; (b) Degraded image with motion kernel (20, 60) and noise level  $\sigma = 25$ ; Restored satellite image by (c) F-ABF [35]; (d) K-QSVD [10,11]; (e) DVTV [36]; (f) BM3D [37]; (g) QNLM [12,13]; (h) QWNNM [15]; (i) adaptive QWNNM (ours).

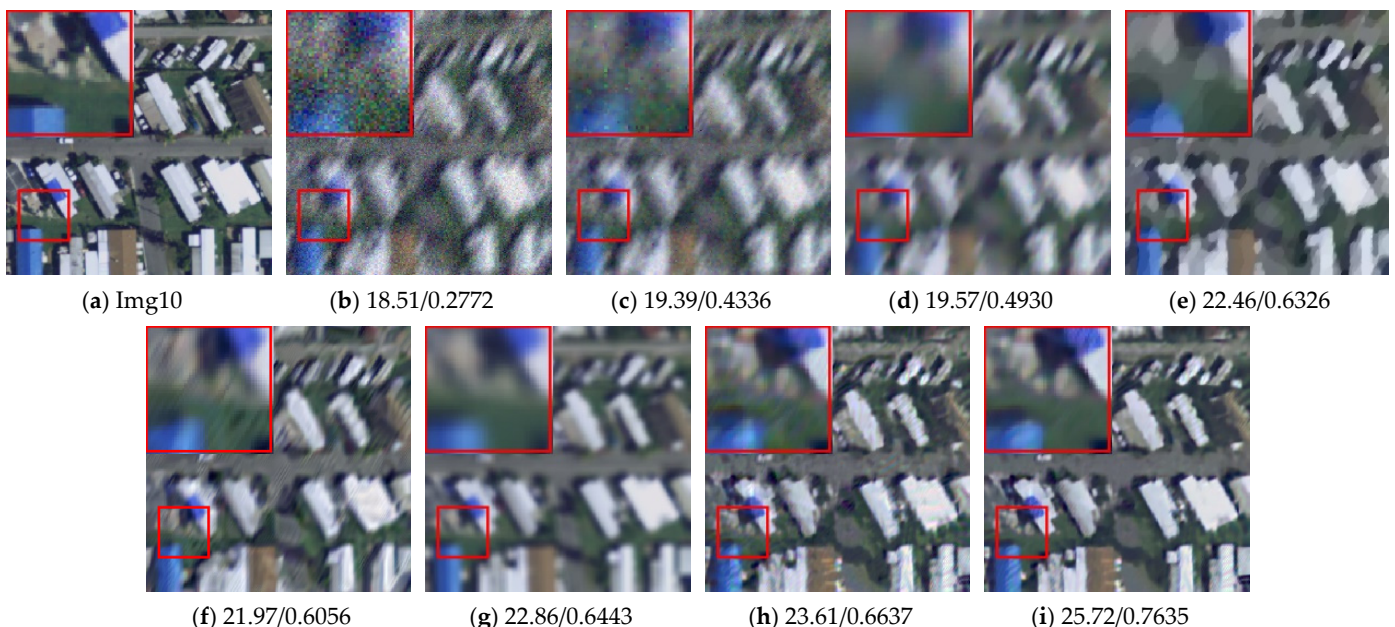


**Figure 10.** Restoration performance on “Img10” with visual quality and numerical results (PSNR/SSIM). (a) Ground truth; (b) Degraded image with motion kernel (20, 60) and noise level  $\sigma = 25$ ; Restored image by (c) F-ABF [35]; (d) K-QSVD [10,11]; (e) DVTV [36]; (f) BM3D [37]; (g) QNLM [12,13]; (h) QWNNM [15]; (i) adaptive QWNNM (ours).



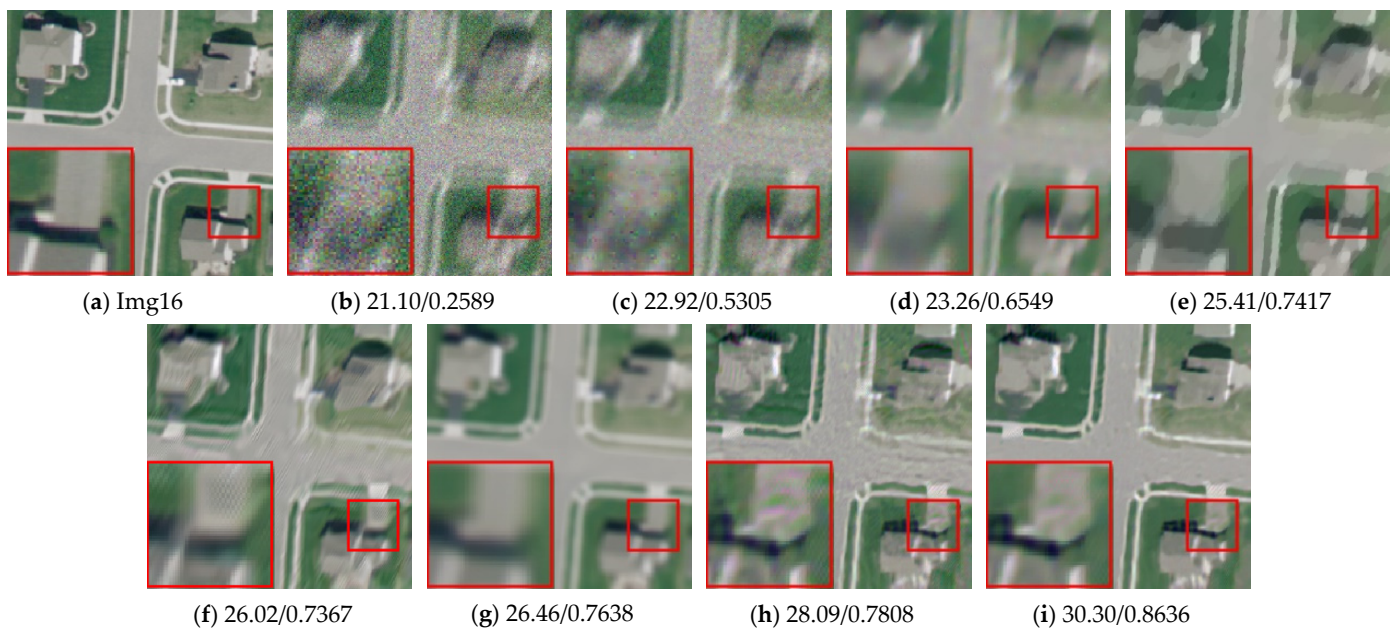


**Figure 11.** Restoration performance on “Img16” with visual quality and numerical results (PSNR/SSIM). (a) Ground truth; (b) Degraded image with motion kernel (20, 60) and noise level  $\sigma = 25$ ; Restored image by (c) F-ABF [35]; (d) K-QSVD [10,11]; (e) DVTV [36]; (f) BM3D [37]; (g) QNLM [12,13]; (h) QWNNM [15]; (i) adaptive QWNNM (ours).

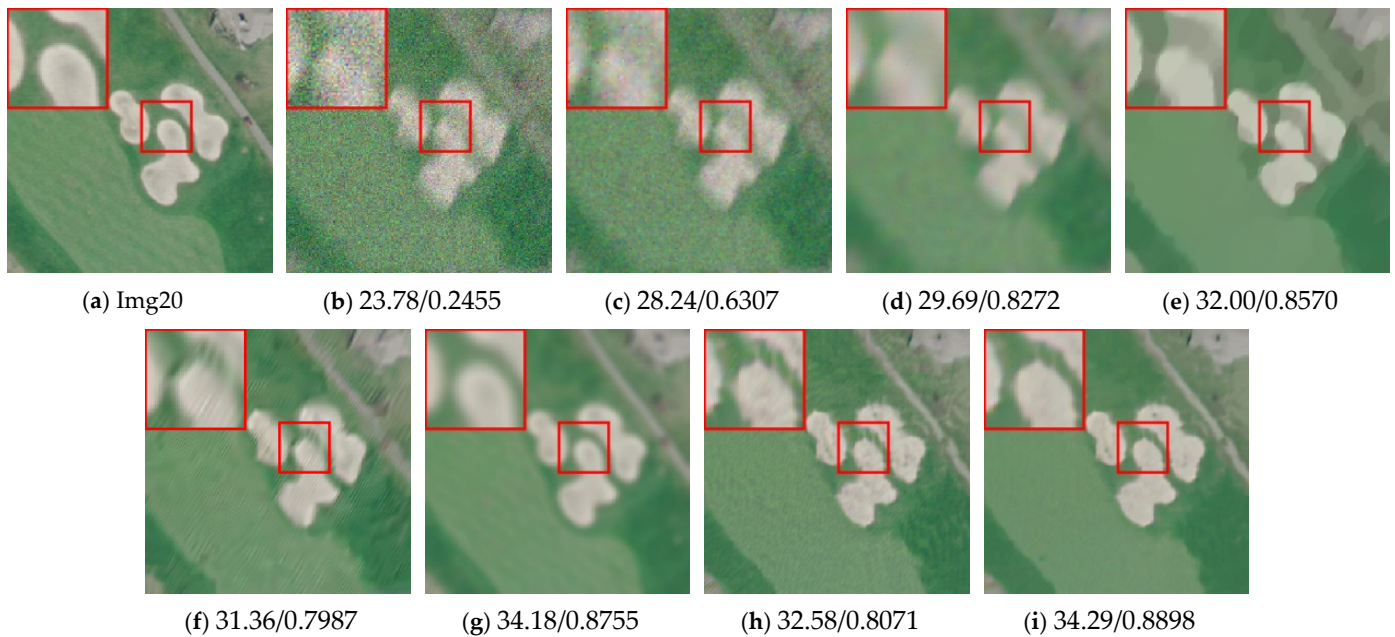


**Figure 12.** Restoration performance on “Img20” with visual quality and numerical results (PSNR/SSIM). (a) Ground truth; (b) Degraded image with motion kernel (20, 60) and noise level  $\sigma = 25$ ; Restored image by (c) F-ABF [35]; (d) K-QSVD [10,11]; (e) DVTV [36]; (f) BM3D [37]; (g) QNLM [12,13]; (h) QWNNM [15]; (i) adaptive QWNNM (ours).

For the restoration of “Img2”, the F-ABF model introduced smoothing distortions and color artifacts, while the K-QSVD model resulted in excessive smoothing that notably blurred the edges of the road, particularly the vertical road markings. The DVTV and BM3D models partially reduced smoothness, while the QNLM and QWNNM models managed to diminish artifacts to some extent but failed to fully restore certain textural features. In contrast, our adaptive QWNNM model exhibited exceptional performance in

satellite image reconstruction. It effectively restored the texture of road signs, removed noise points from the road, and preserved the most distinct details of the digital “36” outline and shadow edges, resulting in a visually appealing and aesthetically pleasing image. The higher PSNR and SSIM values further validated the superiority of our algorithm.

“Img10” represents a satellite image of multiple houses with complex structures, increasing the difficulty of reconstruction. Figure 10 demonstrates the recovery of its degraded image due to motion blur and noise. The F-ABF model introduced additional noise points and color irregularities in the restored image. When the damage to the house image was substantial, the applicability of the F-ABF model became questionable. We selected a clearly defined area within the red box for magnification, and upon close inspection, it is evident that the K-QSVD, DDTV, and BM3D models introduced numerous ringing artifacts in the restored background of the house image, leading to a blurring of the blue boundaries and details. Although the non-local similarity-based QNLM model produced clearer edges, the image remained overly smooth. Compared to the QWNNM model, our proposed model demonstrated greater clarity, enhanced visual quality, and fewer artifacts. It excelled in reducing image noise points, preserving aircraft boundary outlines, and recovering details of airport debris.

‘Img16’ was applied motion blur, simulating rightward movement. F-ABF, K-QSVD, DDTV, and BM3D models struggled to reconstruct the edges and intricate details of the house, as evidenced by the  $2\times$  zoom of the house structure in the lower right corner. The QNLM model excessively smoothed the image, resulting in a substantial loss of critical features. The QWNNM model failed to effectively restore the smoothness of the roads. In contrast, our model accurately captured flat roads and the precise structural details of buildings, successfully preserving grass texture while eliminating undesirable color distortions.

The ‘Img20’ is a satellite image of the golf course. Clearly, the F-ABF, K-QSVD, DDTV, and BM3D models significantly distorted the pseudo color, resulting in highly blurred restored images. Although the QNLM model effectively reconstructed the edges of sand pits, it tended to overly smooth the edges, leading to the loss of critical detail information. While the QWNNM model alleviated some of the excessive smoothing, it still struggled to adequately remove noise and blurring. In contrast, our proposed adaptive QWNNM model excelled in restoring edge information of sand pits within the open spaces of the golf course, not only better preserving details such as the grass color and background but also optimally maintaining the edges of sand pits, providing the most visually pleasing depiction of the golf course.

#### 4.3. Real Environment Experiments with Unknown Noise/Blurring

In this subsection, we conducted restoration experiments on six satellite images (Figure 13) degraded by various noise types in the real environment, including haze, stripes, blurring, etc. We compared our adaptive QWNNM against five advanced techniques: F-ABF [35], K-QSVD [10,11], BM3D [37], QNLM [12,13], and QWNNM [15]. To provide a more objective assessment of reconstruction results, since without ground-truth image as reference, we employed three blind noise metrics: BLIINDS 2 [46], BRISQUE [47], and NIQE [48]. Higher BLIINDS 2 values indicate better restoration results, while the lower BRISQUE and NIQE values signifies the higher the quality of the restoration image. Table 3 summarized BLIINDS 2, BRISQUE, and NIQE values of satellite image restoration experiments by different models. Figures 14–19 compared the visual restoration results by using the competing models. For all three evaluation indices, our proposed model demonstrated significantly improved image restoration performance. This underscores its effectiveness regardless of the noise type present.



**Figure 13.** Satellite images degraded by haze, stripes, and blurring in a real environment, enumerated from left-to-right.

**Table 3.** BLIINDS 2, BRISQUE, and NIQE values of different restoration models (the best result is in bold).

Real Image	Indexes	F-ABF [35]	K-QSVD [10,11]	BM3D [37]	QNLN [12,13]	QWNNM [15]	Proposed
1	BLIINDS 2	35.525	31.078	41.037	24.636	38.536	<b>43.363</b>
	BRISQUE	34.008	29.425	33.929	35.065	32.321	<b>28.860</b>
	NIQE	6.9651	<b>6.8141</b>	10.1083	12.2462	8.9234	7.1641
2	BLIINDS 2	55.528	41.099	57.544	40.574	55.283	<b>58.531</b>
	BRISQUE	42.851	43.830	44.413	51.274	<b>42.028</b>	43.934
	NIQE	7.2057	7.4444	7.2383	9.2311	7.3108	<b>6.6876</b>
3	BLIINDS 2	42.537	35.537	35.272	32.558	43.576	<b>46.550</b>
	BRISQUE	44.309	34.687	32.566	31.243	35.233	<b>32.247</b>
	NIQE	<b>6.6394</b>	8.0520	10.592	10.9544	8.4152	7.0428
4	BLIINDS 2	41.265	46.539	57.502	37.021	55.026	<b>65.195</b>
	BRISQUE	43.458	42.827	43.117	43.373	43.457	<b>41.064</b>
	NIQE	9.2277	9.1812	11.869	9.7100	9.9806	<b>8.2862</b>
5	BLIINDS 2	28.519	31.075	36.046	21.019	41.195	<b>46.502</b>
	BRISQUE	41.876	43.737	42.638	48.459	42.321	<b>41.852</b>
	NIQE	<b>4.7248</b>	6.5645	8.1706	9.5664	8.8154	7.2943
6	BLIINDS 2	35.551	41.179	42.542	32.581	45.079	<b>47.509</b>
	BRISQUE	40.057	38.281	<b>32.903</b>	57.292	37.127	37.912
	NIQE	6.7352	6.1613	6.7624	9.8949	6.5657	<b>5.9813</b>

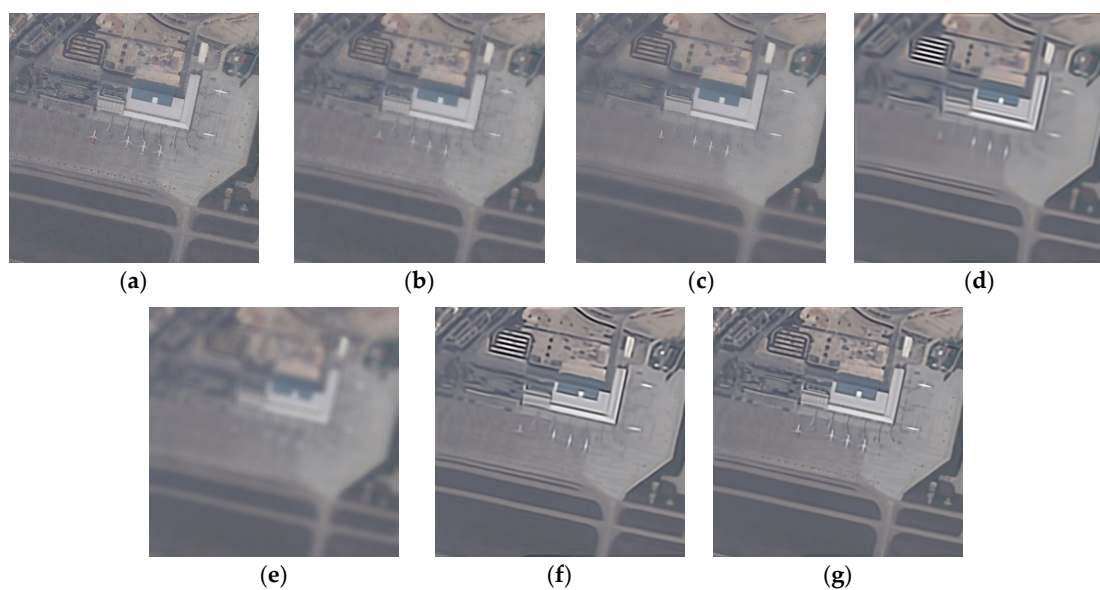


**Figure 14.** Visual quality comparison of original satellite image 1 (a) and restored satellite image by (b) F-ABF [35]; (c) K-QSVD [10,11]; (d) BM3D [37]; (e) QNLN [12,13]; (f) QWNNM [15]; (g) adaptive QWNNM (ours).

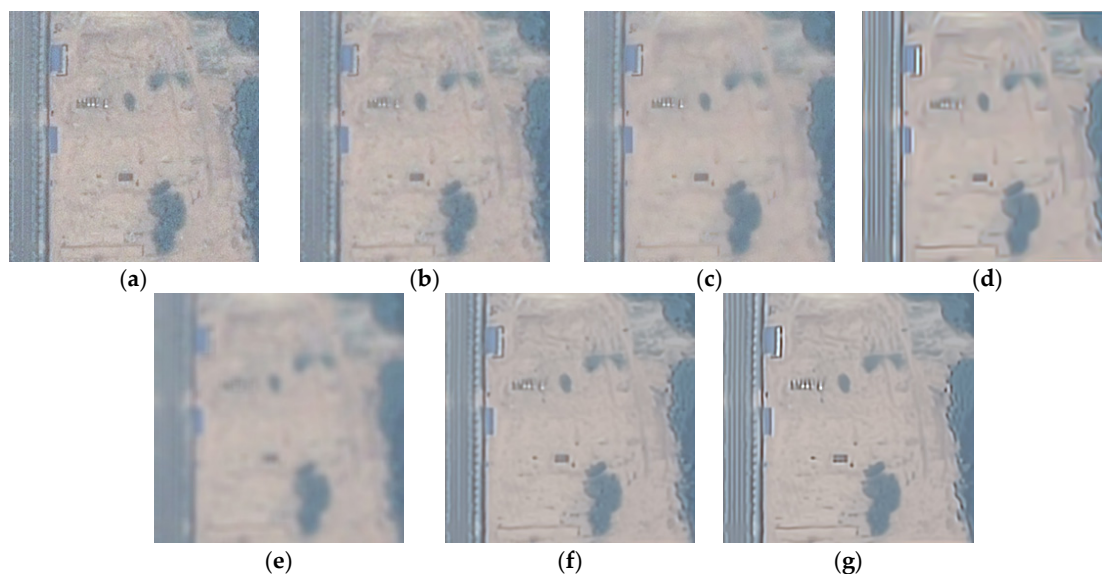


**Figure 15.** Visual quality comparison of original satellite image 2 (a) and restored satellite image by (b) F-ABF [35]; (c) K-QSVD [10,11]; (d) BM3D [37]; (e) QNLM [12,13]; (f) QWNNM [15]; (g) adaptive QWNNM (ours).

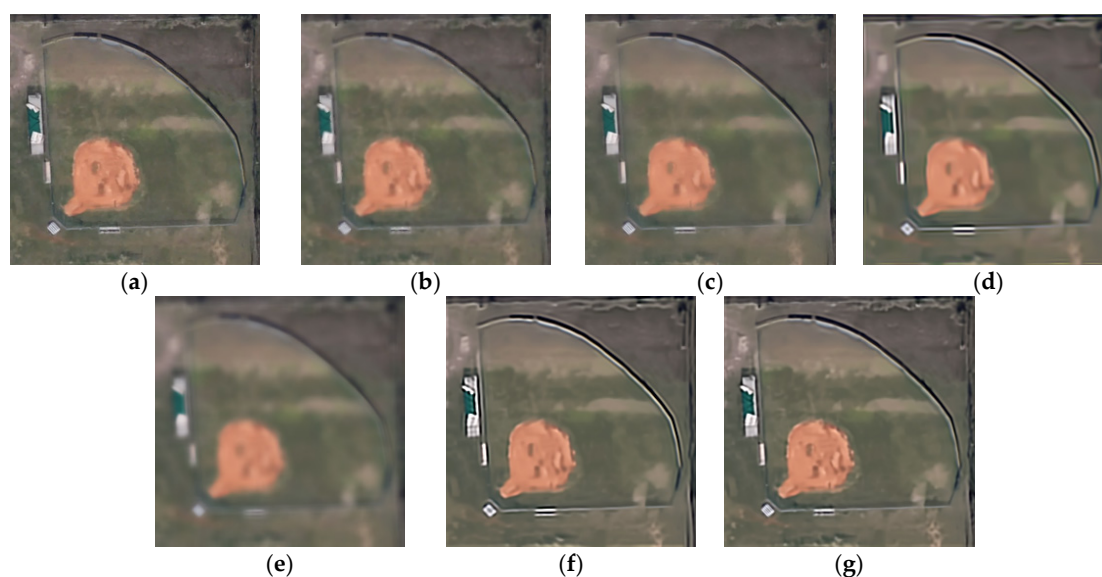


**Figure 16.** Visual quality comparison of original satellite image 3 (a) and restored satellite image by (b) F-ABF [35]; (c) K-QSVD [10,11]; (d) BM3D [37]; (e) QNLM [12,13]; (f) QWNNM [15]; (g) adaptive QWNNM (ours).

The QNLM model (Figures 14e, 15e, 16e, 17e, 18e and 19e) yielded the worst visual results in restored images that are notably blurred and distorted, highlighting the limitations of non-local technique when noise levels are unknown. Similarly, both K-QSVD (Figures 14c, 15c, 16c, 17c, 18c and 19c) and BM3D (Figures 14d, 15d, 16d, 17d, 18d and 19d) models exhibited weaker performance, as their overly smooth restorations failed to preserve important details, such as the small airplane in “Image 1” and the edges of the house in “Image 4”. While BM3D effectively reduced stripe noise in “Image 5”, it still lacked detail retention. The F-ABF model (Figures 14b, 15b, 16b, 17b, 18b and 19b) retained more detail and reduced stripe noise but was less effective against haze, resulting in blur in “Image 1 and image 2”. The QWNNM model (Figures 14f, 15f, 16f, 17f, 18f and 19f) partially mitigated over-smoothing and enhanced clarity, yet it struggled to recover certain textures, exemplified by the small airplane “Image1”. In contrast, our adaptive QWNNM model

(Figures 14g, 15g, 16g, 17g, 18g and 19g) achieved the best visual results overall, preserving intricate details such as the left road in “Image 2”, the patterns of brown soil in “Image 3”, and the triangular pattern on the central square in “Image 6”, while reconstructing the contours and colors of the house in “Image 4” with clarity. These findings demonstrated that our model outperformed five comparative models in removing stripe noise, preserving essential details, and minimizing artifacts, positioning it as a superior option for image restoration in satellite applications, particularly under varying noise conditions.

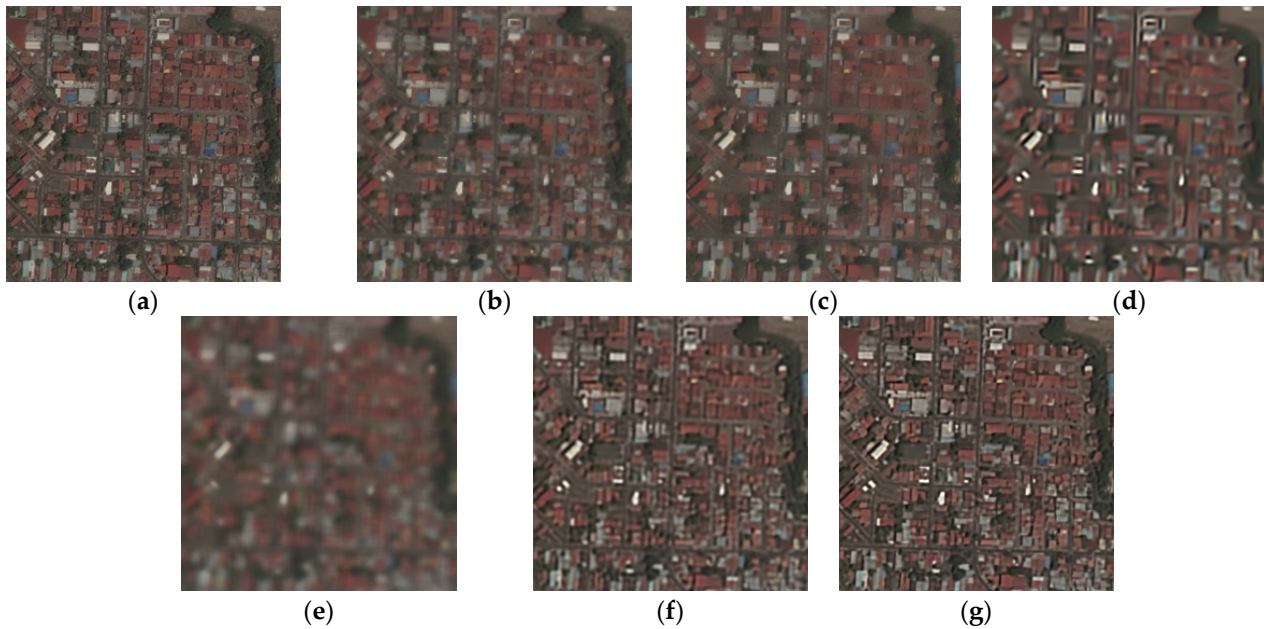


**Figure 17.** Visual quality comparison of original satellite image 4 (a) and restored satellite image by (b) F-ABF [35]; (c) K-QSVD [10,11]; (d) BM3D [37]; (e) QNLM [12,13]; (f) QWNNM [15]; (g) adaptive QWNNM (ours).

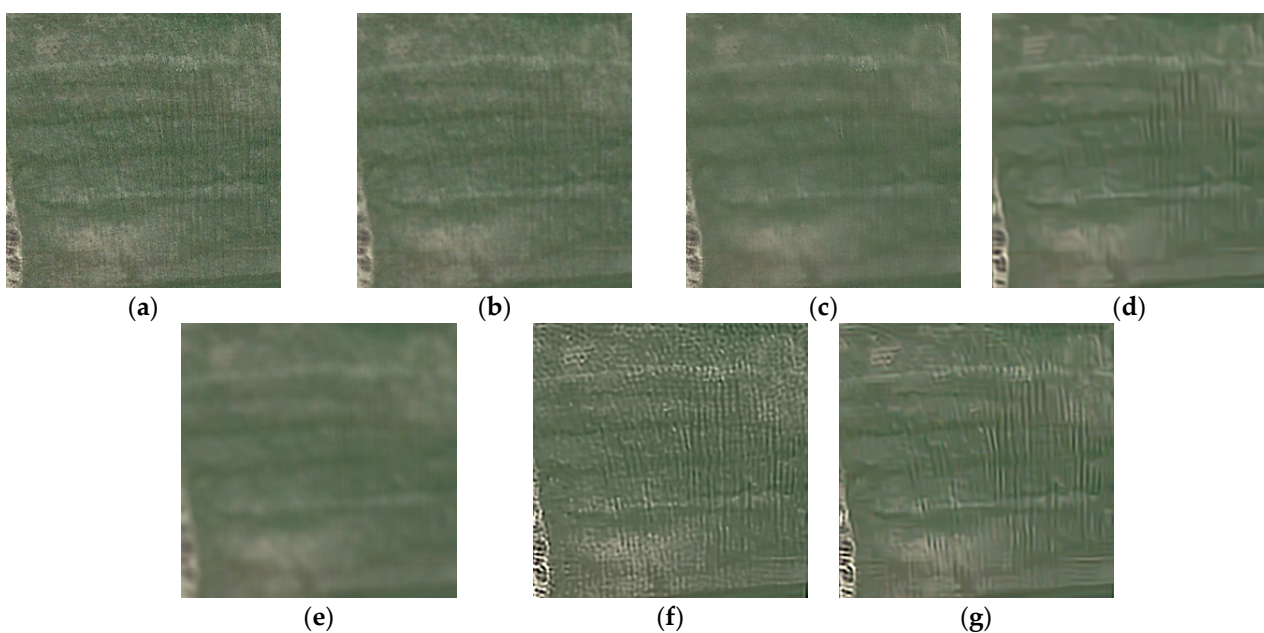


**Figure 18.** Visual quality comparison of original satellite image 5 (a) and restored satellite image by (b) F-ABF [35]; (c) K-QSVD [10,11]; (d) BM3D [37]; (e) QNLM [12,13]; (f) QWNNM [15]; (g) adaptive QWNNM (ours).

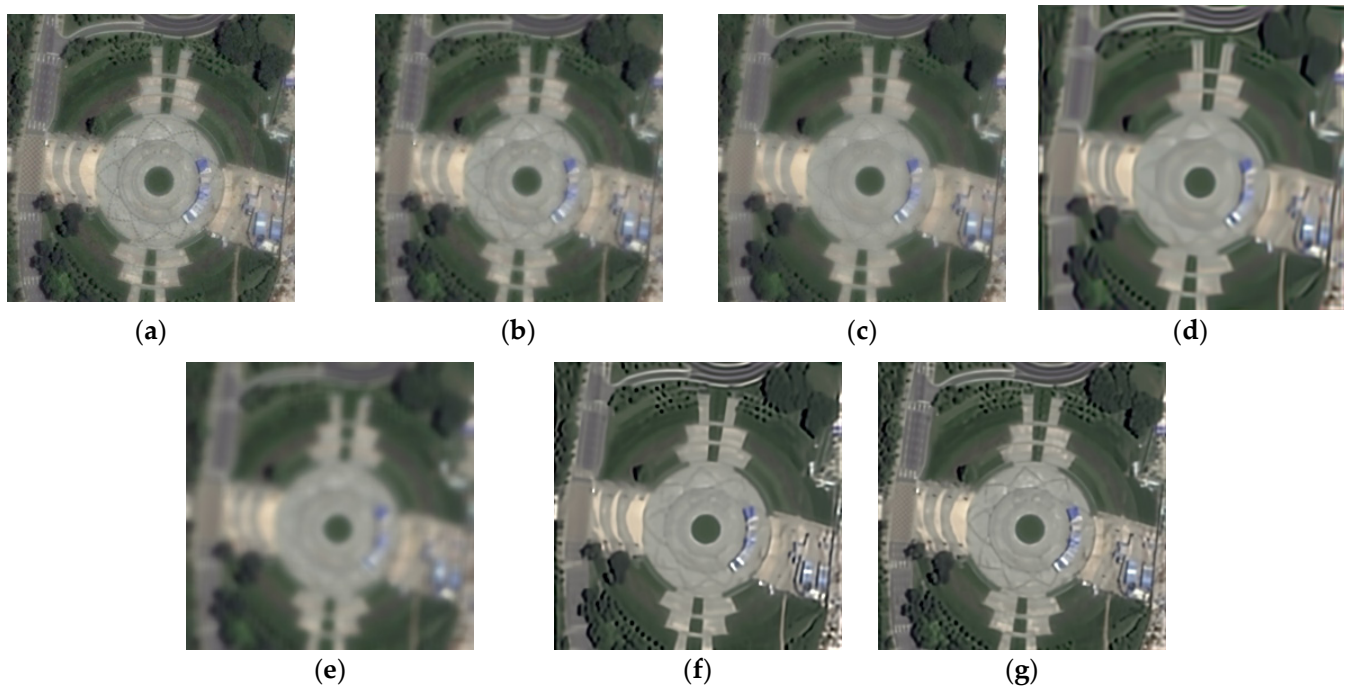


**Figure 19.** Visual quality comparison of original satellite image 6 (a) and restored satellite image by (b) F-ABF [35]; (c) K-QSVD [10,11]; (d) BM3D [37]; (e) QNLM [12,13]; (f) QWNNM [15]; (g) adaptive QWNNM (ours).

#### 4.4. Coupling Effect of Three Adaptive Strategies

In this subsection, we investigate the coupling effects of three adaptive strategies: Adaptive Noise-Resilient Block Matching (S1), Adaptive Feedback of Residual Images (S2), and Adaptive Iteration Stopping Criterion (S3) on the satellite image. Table 4 presents a comparison of the PSNR, SSIM, FSIM, and ERGAS values for the original QWNNM model and different combinations of adaptive strategies (S1, S1&S2, S1&S3, and S1&S2&S3) in terms of image restoration. Figure 20 provides a visual representation of the reconstruction results for the three satellite images.

**Table 4.** Restoration results of three modification for MB(20, 60)/ $\sigma = 25$ .

Images	Metrics	Degraded	QWNNM [15]	S1	S1&S2	S1&S3	Proposed
Runway	PSNR	22.122	26.3670	27.327	30.258	27.770	31.063
	SSIM	0.3935	0.6997	0.7342	0.8099	0.7408	0.8203
	FSIM	0.6790	0.8018	0.8135	0.8651	0.8168	0.8708
	ERGAS	198.28	118.91	104.16	75.52	100.89	70.098
Airport	PSNR	23.9361	28.569	28.837	30.463	28.846	30.604
	SSIM	0.4516	0.7316	0.7441	0.7856	0.7429	0.7862
	FSIM	0.7325	0.8292	0.8139	0.8420	0.8125	0.8413
	ERGAS	190.33	109.61	104.58	86.95	105.05	86.67
Residential	PSNR	23.127	26.505	26.483	28.268	26.483	28.292
	SSIM	0.4166	0.6503	0.6489	0.734	0.6489	0.734
	FSIM	0.7102	0.7967	0.7959	0.8425	0.7959	0.8413
	ERGAS	189.8	129.19	125.46	104.54	125.46	105.25

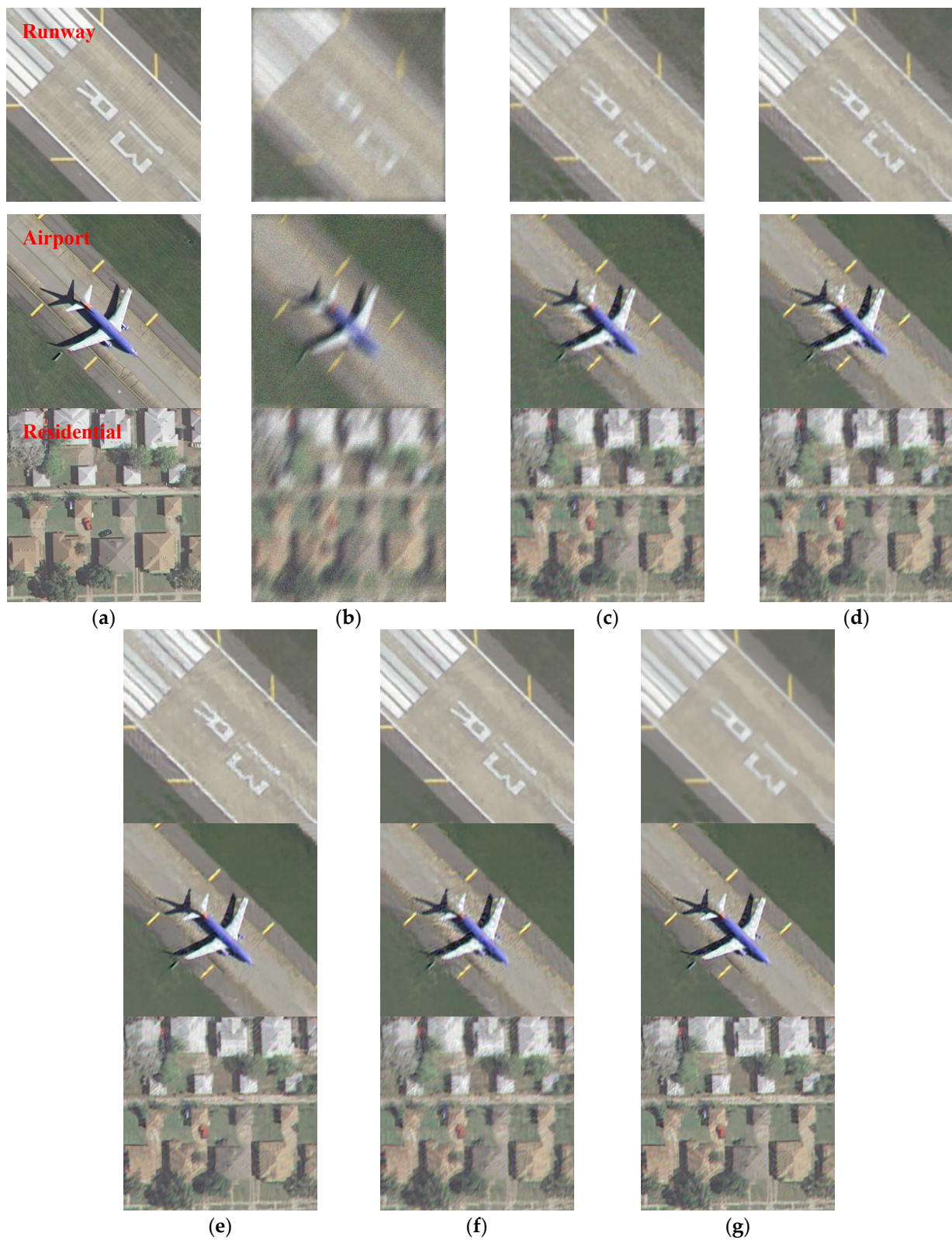


**Figure 20.** Restoration performance with visual quality. (a) Ground truth; (b) Degraded image with motion kernel (20, 60) and noise level 25; Restored satellite image by (c) QWNNM [15]; (d) S1; (e) S1&S2; (f) S1&S3; (g) adaptive QWNNM (S1&S2&S3).

Building upon the original QWNNM model, adding different combinations of adaptive strategies underwent further optimization of restoration performance, particularly

regarding the PSNR, SSIM, FSIM, and ERGAS metrics, with average improvements of 1.589, 0.0510, 0.0205, and  $-19.69$ , respectively. S1 demonstrated improvements across all metrics compared to QWNNM. By transforming image blocks from the traditional spatial domain to the quaternion frequency domain and applying soft-thresholding to shrink the frequency coefficients such that noise components can be effectively suppressed in the similarity measurement, enhancing the accuracy of similarity measurements and then improving image restoration results. S1&S3 achieved the similar restoration performance as that in S1. This is because the incorporation of Adaptive Iteration Stopping Criterion (S3) is to reduce the number of iterations (i.e., computational complex). In contrast, S1&S2 demonstrated greater improvements, particularly in the clarity of the “R13” road sign in the “Runway”, the blue fuselage of the aircraft in the “ Airport “, and the contours of the houses in the “Residential” (Figure 20), indicating that the inclusion of edge information in residual images achieved comprehensive enhancements over the original QWNNM model. Overall, the adaptive QWNNM model (S1&S2&S3) excelled across all metrics, making it the most effective option. In terms of overall visual quality and detail representation, it closely resembles the original image state, effectively demonstrating the efficacy and practicality of the adaptive QWNNM model in satellite image restoration.

## 5. Conclusions

Due to channel noise and random atmospheric turbulence, retrieved satellite images are always distorted and degraded and so require further restoration before use in various applications. In this study, we present an adaptive quaternion-weighted nuclear norm minimization model, which offers several advantageous features. First, our model integrated the benefits of quaternion representation and soft thresholding in the frequency domain, providing a novel approach to mitigate noise impacts in block matching. Second, our model incorporated an adaptive proportion of the residual image from each iteration as feedback in the next iteration, allowing to use edge information in residual images to continuously improve the restoration performance during the iterative process. Finally, our model established a stopping criterion of iteration processes through measuring the dependence between the current restored image and the corresponding residual image. Both simulation experiments with known noise/blurring and real environment experiments with unknown noise/blurring confirmed the effectiveness and robustness of our adaptive QWNNM model over the original QWNNM model and other state-of-the-art restoration models in very different technique approaches.

**Author Contributions:** X.X. and Z.Z. are co-first author. Conceptualization, Z.Z.; Methodology, X.X. and Z.Z.; Software, X.X.; Validation, X.X.; Formal analysis, X.X. and Z.Z.; Investigation, M.J.C.C.; Writing—original draft, X.X. and Z.Z.; Writing—review & editing, Z.Z. and M.J.C.C. All authors have read and agreed to the published version of the manuscript.

**Funding:** The corresponding author was supported by the European Commission Horizon 2020 Framework Program No. 861584 and the Taishan Distinguished Professor Fund No. 20190910.

**Data Availability Statement:** Data are contained within the article.

**Conflicts of Interest:** The authors declare no conflicts of interest.

## References

1. Zhang, X.; Zheng, J.; Wang, D.; Zhao, L. Exemplar-Based Denoising: A Unified Low-Rank Recovery Framework. *IEEE Trans. Circuits Syst. Video Technol.* **2020**, *30*, 2538–2549. [[CrossRef](#)]
2. Zarmehi, N.; Amini, A.; Marvasti, F. Low Rank and Sparse Decomposition for Image and Video Applications. *IEEE Trans. Circuits Syst. Video Technol.* **2020**, *30*, 2046–2056. [[CrossRef](#)]
3. Guo, Q.; Gao, S.; Zhang, X.; Yin, Y.; Zhang, C. Patch-Based Image Inpainting via Two-Stage Low Rank Approximation. *IEEE Trans. Vis. Comput. Graph.* **2018**, *24*, 2023–2036. [[CrossRef](#)]
4. Candès, E.; Recht, B. Exact Matrix Completion via Convex Optimization. *Commun. ACM* **2012**, *55*, 111–119. [[CrossRef](#)]
5. Candès, E.J.; Tao, T. The Power of Convex Relaxation: Near-Optimal Matrix Completion. *IEEE Trans. Inf. Theory* **2010**, *56*, 2053–2080. [[CrossRef](#)]



6. Cai, J.F.; Candès, E.J.; Shen, Z. A Singular Value Thresholding Algorithm for Matrix Completion. *SIAM J. Optim.* **2010**, *20*, 1956–1982. [[CrossRef](#)]
7. Gu, S.; Xie, Q.; Meng, D.; Zuo, W.; Feng, X.; Zhang, L. Weighted Nuclear Norm Minimization and Its Applications to Low Level Vision. *Int. J. Comput. Vis.* **2017**, *121*, 183–208. [[CrossRef](#)]
8. Luisier, F.; Blu, T. SURE-LET Multichannel Image Denoising: Interscale Orthonormal Wavelet Thresholding. *IEEE Trans. Image Process.* **2008**, *17*, 482–492. [[CrossRef](#)]
9. Dabov, K.; Foi, A.; Katkovnik, V.; Egiazarian, K. Image Denoising by Sparse 3-D Transform-Domain Collaborative Filtering. *IEEE Trans. Image Process.* **2007**, *16*, 2080–2095. [[CrossRef](#)]
10. Carmeli, A.; Turek, J. Quaternion K-SVD for Color Image Denoising. *Tech. Isr. Inst. Technol. Tech. Rep.* **2013**. Available online: <https://api.semanticscholar.org/CorpusID:15559041> (accessed on 1 August 2024).
11. Xu, Y.; Yu, L.; Xu, H.; Zhang, H.; Nguyen, T. Vector Sparse Representation of Color Image Using Quaternion Matrix Analysis. *IEEE Trans. Image Process.* **2015**, *24*, 1315–1329. [[CrossRef](#)] [[PubMed](#)]
12. Wang, G.; Liu, Y.; Xiong, W.; Li, Y. An improved non-local means filter for color image denoising. *Opt.-Int. J. Light Electron Opt.* **2018**, *173*, 157–173. [[CrossRef](#)]
13. Jia, Z.; Jin, Q.; Ng, M.K.; Zhao, X.L. Non-Local Robust Quaternion Matrix Completion for Large-Scale Color Image and Video Inpainting. *IEEE Trans. Image Process.* **2022**, *31*, 3868–3883. [[CrossRef](#)] [[PubMed](#)]
14. Yu, Y.; Zhang, Y.; Yuan, S. Quaternion-Based Weighted Nuclear Norm Minimization for Color Image Denoising. *Neurocomputing* **2019**, *332*, 283–297. [[CrossRef](#)]
15. Huang, C.; Li, Z.; Liu, Y.; Wu, T.; Zeng, T. Quaternion-Based Weighted Nuclear Norm Minimization for Color Image Restoration. *Pattern Recognit.* **2022**, *128*, 108665. [[CrossRef](#)]
16. Huang, C.; Li, J.; Gao, G. Review of Quaternion-Based Color Image Processing Methods. *Mathematics* **2023**, *11*, 2056. [[CrossRef](#)]
17. Miao, J.; Kou, K.I. Color Image Recovery Using Low-Rank Quaternion Matrix Completion Algorithm. *IEEE Trans. Image Process.* **2022**, *31*, 190–201. [[CrossRef](#)]
18. Maheswari, C.; Gowthami, K.N.B.; Reddy, V.M. Salient Region Detection Based on Frequency Domain Analysis for Remote Sensing Image. *Adv. Electron. Electr. Eng.* **2023**, *14*, 15–26.
19. El Alami, A.; Mesbah, A.; Berrahou, N.; Lakhili, Z.; Berrahou, A.; Qjidaa, H. Quaternion Discrete Orthogonal Hahn Moments Convolutional Neural Network for Color Image Classification and Face Recognition. *Multimed. Tools Appl.* **2023**, *82*, 32827–32853. [[CrossRef](#)]
20. Zhang, H.; Qi, T.; Zeng, T. Quaternion-Aware Low-Rank Prior for Blind Color Image Deblurring. *J. Sci. Comput.* **2024**, *101*, 27. [[CrossRef](#)]
21. Chen, J.; Huang, G.; Yuan, X.; Zhong, G.; Zheng, Z.; Pun, C.-M.; Zhu, J.; Huang, Z. Quaternion Cross-Modality Spatial Learning for Multi-Modal Medical Image Segmentation. *IEEE J. Biomed. Health Inform.* **2024**, *28*, 1412–1423. [[CrossRef](#)] [[PubMed](#)]
22. Cheng, Y.; Ling, B.W.-K.; Lin, Y.; Huang, Z.; Chan, Y.-L. Image Super Resolution via Combination of Two Dimensional Quaternion Valued Singular Spectrum Analysis Based Denoising, Empirical Mode Decomposition Based Denoising and Discrete Cosine Transform Based Denoising Methods. *Multimed. Tools Appl.* **2023**, *82*, 22705–22722. [[CrossRef](#)]
23. Yang, L.; Liu, Y.; Kou, K.I. Quaternion Optimized Model with Sparseness for Color Image Recovery. *Digit. Signal Prog.* **2025**, *156*, 104781. [[CrossRef](#)]
24. MacQueen, J. Some Methods for Classification and Analysis of Multivariate Observations. In Proceedings of the fifth Berkeley Symposium on Mathematical Statistics & Probability, Berkeley, CA, USA, 21 June–18 July 1967; pp. 281–297.
25. Tamayo, P.; Slonim, D.; Mesirov, J.; Zhu, Q.; Kitareewan, S.; Dmitrovsky, E.; Lander, E.S.; Golub, T.R. Interpreting Patterns of Gene Expression with Self-Organizing Maps: Methods and Application to Hematopoietic Differentiation. *Proc. Natl. Acad. Sci. USA* **1999**, *96*, 2907–2912. [[CrossRef](#)]
26. Peters, R.M.; Shaniy, S.A.; Peters, J.C. Fuzzy Cluster Analysis: A New Method to Predict Future Cardiac Events in Patients with Positive Stress Tests. *Jpn Circ. J.* **1998**, *62*, 750–754. [[CrossRef](#)]
27. Gersho, A. On the Structure of Vector Quantizers. *IEEE Trans. Inf. Theory* **1982**, *28*, 157–166. [[CrossRef](#)]
28. Candès, E.J.; Li, X.; Ma, Y.; Wright, J. Robust Principal Component Analysis? *J. ACM* **2011**, *58*, 1–37. [[CrossRef](#)]
29. Liu, R.; Lin, Z.; Fernando, D.L.T.; Su, Z. Fixed-Rank Representation for Unsupervised Visual Learning. In Proceedings of the 2012 IEEE Computer Society Conference on Computer Vision and Pattern Recognition, Providence, RI, USA, 16–21 June 2012. [[CrossRef](#)]
30. Zhang, F. Quaternions and Matrices of Quaternions. *Linear Algebra Its Appl.* **1997**, *251*, 21–57. [[CrossRef](#)]
31. Chen, Y.; Jia, Z.; Peng, Y.; Peng, Y. Robust Dual-Color Watermarking Based on Quaternion Singular Value Decomposition. *IEEE Access* **2020**, *8*, 30628–30642. [[CrossRef](#)]
32. Guo, H.; Wu, X.; Cai, S.; Li, N.; Cheng, J.; Chen, Y. Quaternion Discrete Cosine Transformation Signature Analysis in Crowd Scenes for Abnormal Event Detection. *Neurocomputing* **2016**, *204*, 106–115. [[CrossRef](#)]
33. Schauerte, B.; Stiefelhagen, R. Predicting Human Gaze Using Quaternion DCT Image Signature Saliency and Face Detection. In Proceedings of the 2012 IEEE Workshop on the Applications of Computer Vision (WACV), Breckenridge, CO, USA, 9–11 January 2012.
34. Canny, J. A Computational Approach to Edge Detection. *IEEE Trans. Pattern Anal. Mach. Intell.* **1986**, *PAMI-8*, 679–698. [[CrossRef](#)]

35. Gavaskar, R.G.; Chaudhury, K.N. Fast Adaptive Bilateral Filtering. *IEEE Trans. Image Process. Publ. IEEE Signal Process. Soc.* **2019**, *28*, 779–790. [[CrossRef](#)] [[PubMed](#)]
36. Ono, S.; Yamada, I. Decorrelated Vectorial Total Variation. In Proceedings of the 2014 IEEE Conference on Computer Vision and Pattern Recognition, Columbus, OH, USA, 23–28 June 2014; pp. 4090–4097.
37. Makinen, Y.; Azzari, L.; Foi, A. Exact Transform-Domain Noise Variance for Collaborative Filtering of Stationary Correlated Noise. In Proceedings of the 2019 IEEE International Conference on Image Processing (ICIP), Taipei, Taiwan, 22–25 September 2019.
38. Golilarz, N.A.; Mirmozaffari, M.; Gashteroodkhani, T.A.; Ali, L.; Dolatsara, H.A.; Boskabadi, A.; Yazdi, M. Optimized Wavelet-Based Satellite Image De-Noising with Multi-Population Differential Evolution-Assisted Harris Hawks Optimization Algorithm. *IEEE Access* **2020**, *8*, 133076–133085. [[CrossRef](#)]
39. Liu, H.; Li, Z.; Lin, S.; Cheng, L. Remote Sensing Image Denoising Based on Deformable Convolution and Attention-Guided Filtering in Progressive Framework. *Signal Image Video Process.* **2024**, *18*, 8195–8205. [[CrossRef](#)]
40. Yang, X.; Xie, T.; Guo, Y.; Zhou, D. Remote Sensing Image Super-resolution Based on Convolutional Blind Denoising Adaptive Dense Connection. *IET Image Process.* **2021**, *15*, 2508–2520. [[CrossRef](#)]
41. Yang, Y.; Newsam, S. Bag-of-Visual-Words and Spatial Extensions for Land-Use Classification. In Proceedings of the 18th SIGSPATIAL International Conference on Advances in Geographic Information Systems, San Jose, CA, USA, 2–5 November 2010; Association for Computing Machinery: New York, NY, USA, 2010; pp. 270–279.
42. Slanina, M. Estimating PSNR in High Definition H.264/AVC Video Sequences Using Artificial Neural Networks. *Radioengineering* **2008**, *17*, 103–108.
43. Wang, Z.; Bovik, A.C.; Sheikh, H.R.; Simoncelli, E.P. Image Quality Assessment: From Error Visibility to Structural Similarity. *IEEE Trans. Image Process.* **2004**, *13*, 600–612. [[CrossRef](#)]
44. Zhang, L.; Zhang, L.; Mou, X.; Zhang, D. FSIM: A Feature Similarity Index for Image Quality Assessment. *IEEE Trans. Image Process.* **2011**, *20*, 2378–2386. [[CrossRef](#)]
45. Wald, L. *Data Fusion. Definitions and Architectures-Fusion of Images of Different Spatial Resolutions*; Presses des MINES: Paris, France, 2010.
46. Saad, M.A.; Bovik, A.C.; Charrier, C. Blind Image Quality Assessment: A Natural Scene Statistics Approach in the DCT Domain. *IEEE Trans. Image Process.* **2012**, *21*, 3339–3352. [[CrossRef](#)]
47. Gupta, P.; Moorthy, A.K.; Soundararajan, R.; Bovik, A.C. Generalized Gaussian Scale Mixtures: A Model for Wavelet Coefficients of Natural Images. *Signal Process. Image Commun.* **2018**, *66*, 87–94. [[CrossRef](#)]
48. Gu, K.; Tao, D.; Qiao, J.F.; Lin, W. Learning a No-Reference Quality Assessment Model of Enhanced Images with Big Data. *IEEE Trans. Neural Netw. Learn. Syst.* **2017**, *29*, 1301–1313. [[CrossRef](#)] [[PubMed](#)]

**Disclaimer/Publisher’s Note:** The statements, opinions and data contained in all publications are solely those of the individual author(s) and contributor(s) and not of MDPI and/or the editor(s). MDPI and/or the editor(s) disclaim responsibility for any injury to people or property resulting from any ideas, methods, instructions or products referred to in the content.